PHYSICAL REVIEW FLUIDS **5**, 084601 (2020)

Spectra and scaling in chemically reacting compressible isotropic turbulence

Jian Teng,[1,2,3,4] Jianchun Wang,[1,3,4,*] Hui Li,[2] and Shiyi Chen[1,3,4,†]
[1]*Shenzhen Key Laboratory of Complex Aerospace Flows, Center for Complex Flows and Soft Matter Research, Department of Mechanics and Aerospace Engineering, Southern University of Science and Technology, Shenzhen, Guangdong 518055, People's Republic of China*
[2]*School of Power and Mechanical Engineering, Wuhan University, Wuhan 430072, People's Republic of China*
[3]*Southern Marine Science and Engineering Guangdong Laboratory, Guangzhou, 511458, People's Republic of China*
[4]*Guangdong Provincial Key Laboratory of Turbulence Research and Applications, Department of Mechanics and Aerospace Engineering, Southern University of Science and Technology, Shenzhen, Guangdong 518055, People's Republic of China*

(Received 20 March 2020; accepted 8 July 2020; published 4 August 2020)

Numerical simulations are carried out to study the spectra and statistics in chemically reacting compressible homogeneous isotropic turbulence at turbulent Mach number M_t from 0.1 to 1.0 and at Taylor Reynolds number Re_λ from 54 to 103 with solenoidal forcing. A single-step irreversible Arrhenius-type chemical reaction is implemented to evaluate the influence of chemical reaction on spectra and flow statistics. It is shown that in the situation of isothermal reactions, both the ratio of compressible kinetic energy to solenoidal kinetic energy K^c/K^s and the ratio of compressible dissipation to solenoidal dissipation ϵ^c/ϵ^s exhibit a M_t^4 scaling at low turbulent Mach numbers $M_t < 0.4$. At $M_t \geqslant 0.4$, K^c/K^s and ϵ^c/ϵ^s exhibit M_t^2 and M_t^5 scaling behaviors, respectively, and the flow is in strong acoustic equilibrium. The spectra of velocity, pressure, density, and temperature are nearly unaffected by the isothermal chemical reaction. In contrast, heat release in exothermal reactions significantly enhances the spectra of velocity and thermodynamic variables in a wide range of length scales. It is found that the spectra of pressure and compressible velocity satisfy the strong acoustic equilibrium relation at M_t from 0.1 to 0.6, indicating that the acoustic mode dominates over the dynamics of compressible velocity and pressure. In the situation of exothermal reactions, K^c/K^s and ϵ^c/ϵ^s appear to be independent of turbulent Mach number. The normalized root-mean-square values of pressure, density, and temperature exhibit a M_t^2 scaling in the isothermal reactions and exhibit a M_t scaling in the exothermal reactions.

DOI: 10.1103/PhysRevFluids.5.084601

I. INTRODUCTION

Turbulent reactive flows are commonly observed in chemical reactive devices, energy generation plants, and combustion engines [1–3]. Interaction between turbulent flows and chemical reactions over a wide range of time and length scales exerts a significant influence on dynamical evolution of flow quantities and energy transfer [4–6]. The complex turbulence-chemistry interaction poses great challenges in understanding the nonlinear nature of turbulence in coupling with chemical reaction kinetics [7–9].

---

[*] Corresponding author: wangjc@sustech.edu.cn
[†] Corresponding author: chensy@sustech.edu.cn

Previous explorations of turbulence-chemistry interaction provided meaningful results to unveil the complicated interaction mechanisms through extensive direct numerical simulation (DNS) of forced, decay, and shear chemically reacting turbulence, and identified two types of interaction mechanisms [10–15]. For the first type of interaction mechanism, heat release through exothermic reactions primarily intensifies dilatational motion at all length scales [6,12,16]. The solenoidal velocity field is mainly affected at small scales due to the change of molecular diffusivity and temperature fluctuation [10,12]. The nonuniform heat release into the flow through reactions can greatly intensify pressure, density, and temperature fluctuations [4,17]. Jaberi [4] analyzed weakly compressible reacting isotropic turbulence through a DNS database and found that energy from chemical reactions is basically transferred to the compressible component of kinetic energy through pressure work and is further transferred from the compressible mode to the solenoidal mode through advection. Paes [6] showed that in strong heat release reactions, pressure work dominates turbulent kinetic energy transfer over a wide range of scales. Though the viscous dissipation can also be intensified by heat release, the magnitude is relatively small compared with pressure dilatation [4]. For the second type of interaction mechanism, turbulent motion can affect chemical reactions. In reacting systems, the scalar mixing can be significantly enhanced by turbulent fluctuations [8,18,19]. The location of the intense reaction rate is strongly related with the strength of reactant concentration gradients, which is more likely to be aligned with the direction of the most compressive local strain rate [8]. In addition, it was found that the location of the maximum strain rate determines the location of the maximum reaction rate [8,20].

Early theoretical works by Eschenroeder [21] and Chakraborty [22] concluded that the spectral distributions of turbulent kinetic energy can be affected by reaction heat at small wave numbers. The energy spectra can be distorted due to the present of source terms and inertial transfer of kinetic energy for the exothermal reactions. In recent years, the availability of extensive DNS databases provided opportunities to further explore the nonlinear coupling between velocity and thermodynamic variables in compressible isotropic turbulence and gave physical insight into spectral distributions of velocity and thermodynamic variables. Various scaling behaviors of spectra of compressible velocity component and thermodynamic variables have been identified at turbulent Mach number up to 1.0 in nonreacting turbulence [23–28]. However, systematic investigations of spectra in coupling with chemical reactions over a wide range of scales are insufficient, and thus in-depth analysis is required.

Many previous works have been devoted to the statistics and structures of compressible components of compressible turbulent flows. Ristorcelli [26] suggested a pseudosound theory to characterize compressible turbulence at relatively small turbulent Mach number in which the compressible component of the velocity field can be fully determined through the solenoidal components of velocity and pressure. Sarkar [27] proposed an acoustic wave theory which indicates an equipartition relation between the kinetic energy and the potential energy of the compressible components of flow field. A recent work by Wang [28] further showed that the pseudosound mode and acoustic mode can coexist in weakly compressible turbulence, and a critical wave number k_c can be identified for the transition between two modes. Nevertheless, the statistical properties of compressible components of flow fields in chemically reacting compressible isotropic turbulence are still unclear.

The current study aims to explore the statistical properties of chemically reacting compressible isotropic turbulence and to address the effects of heat release and compressibility on reaction characteristics, flow structures, and spectra of velocity as well as thermodynamic variables. The rest of the paper is organized as follows. In Sec. II the governing equations are presented, and the computational strategy is elaborated. The overall reaction characteristics and typical flow statistics are presented in Sec. III. Spectra of velocity, pressure, temperature, and density are presented in Sec. IV. In Sec. V one-point statistics and Mach number scaling of kinetic energy ratio, dissipation ratio, and root-mean-squared (rms) values of thermodynamic variables are investigated. A summary of major findings and conclusions are provided in Sec. VI.

II. GOVERNING EQUATIONS AND NUMERICAL STRATEGY

The following chemically reacting dimensionless Navier-Stokes equations in conservative form are solved numerically in this study:

$$\frac{\partial \rho}{\partial t}+\frac{\partial(\rho u_j)}{\partial x_j}=0, \tag{1}$$

$$\frac{\partial(\rho u_i)}{\partial t}+\frac{\partial(\rho u_i u_j+p\delta_{ij})}{\partial x_j}=\frac{1}{\mathrm{Re}}\frac{\partial \sigma_{ij}}{\partial x_j}+\mathcal{F}_i, \tag{2}$$

$$\frac{\partial \mathcal{E}}{\partial t}+\frac{\partial[(\mathcal{E}+p)u_j]}{\partial x_j}=\frac{1}{\alpha}\frac{\partial}{\partial x_j}\left(\kappa\frac{\partial T}{\partial x_j}\right)+\frac{1}{\mathrm{Re}}\frac{\partial(\sigma_{ij}u_i)}{\partial x_j}+Q-\Lambda+\mathcal{F}_j u_j, \tag{3}$$

$$\frac{\partial(\rho Y_s)}{\partial t}+\frac{\partial(\rho Y_s u_j)}{\partial x_j}=\frac{1}{\mathrm{Re}}\frac{1}{\mathrm{Sc}}\frac{\partial}{\partial x_j}\left(\mu\frac{\partial Y_s}{\partial x_j}\right)+\dot{\omega}_s,\ s=1,2,\dots,n_s-1, \tag{4}$$

$$p=\rho T/(\gamma M^2), \tag{5}$$

where ρ is the mixture density, u_i is the velocity component, p is the mixture pressure, and T is the temperature. The viscous stress σ_{ij} is defined by

$$\sigma_{ij}=\mu\left(\frac{\partial u_i}{\partial x_j}+\frac{\partial u_j}{\partial x_i}\right)-\frac{2}{3}\mu\theta\delta_{ij}. \tag{6}$$

Here $\theta=\partial u_k/\partial x_k$ is the velocity divergence, Q is heat of the reaction, Y_s is the species mass fraction, $\dot{\omega}_s$ is the species production rate, and n_s is the total number of species in the mixture.

The total energy per unit volume $\mathcal{E}$ is defined by

$$\mathcal{E}=\frac{p}{\gamma-1}+\frac{1}{2}\rho(u_j u_j). \tag{7}$$

A set of reference scales have been used to normalize the hydrodynamic and thermodynamic variables in chemically reacting compressible turbulence, including the reference length L_f, velocity U_f, time L_f/U_f, density ρ_f, pressure $p_f=\rho_f U_f^2$, temperature T_f, energy per unit volume $\rho_f U_f^2$, viscosity μ_f, thermal conductivity κ_f, and molecular weight W_f. After normalization, three reference governing parameters are obtained: the reference Reynolds number $\mathrm{Re}=\rho_f U_f L_f/\mu_f$, the reference Mach number $M=U_f/c_f$, and the reference Prandtl number $\mathrm{Pr}=\mu_f C_p/\kappa_f$. Here the speed of sound is defined by $c_f=\sqrt{\gamma R T_f}$; $\gamma=C_p/C_v$ is the ratio of specific heat at constant pressure C_p to that at constant volume C_v, which is assumed to be equal to 1.4, and R is the specific gas constant. The parameter α is defined by $\alpha=\mathrm{PrRe}(\gamma-1)M^2$. The Schmidt number $\mathrm{Sc}=\mu_f/\rho_f D_f$, where D_f is mass diffusivity proportional to $T_f^{3/2}/p_f$ for gas. It is assumed that the parameters $\mathrm{Pr}=\mathrm{Sc}=0.7$ and the gas is calorically perfect [10,12,29].

Sutherland's law is adopted for calculation of the nondimensional temperature-dependent viscosity coefficient and thermal conductivity coefficient [29]. $\mathcal{F}_i$ is a large-scale forcing and is added to the fluid momentum, and Λ is a large-scale cooling function per unit volume. The large-scale forcing is applied to the solenoidal velocity component by fixing the velocity spectrum within the two lowest wave number shells [29–31]. The spatially uniform thermal cooling is utilized to sustain the internal energy in a statistically steady state [29].

The Taylor microscale Reynolds number Re_λ and the turbulent Mach number M_t are defined, respectively, by [32]

$$\mathrm{Re}_\lambda=\mathrm{Re}\frac{\langle\rho\rangle u'\lambda}{\sqrt{3}\langle\mu\rangle},\quad M_t=M\frac{u'}{\langle\sqrt{T}\rangle}, \tag{8}$$

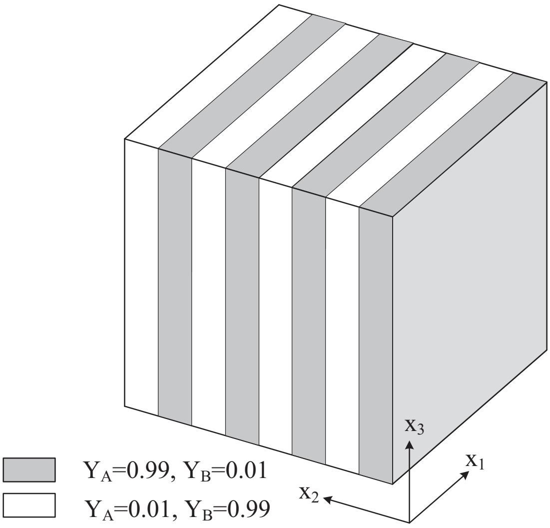

FIG. 1. Initial density field at the start of chemical reaction.

where $\langle\rangle$ stands for spatial average. The rms velocity magnitude is $u' = \sqrt{\langle u_1^2 + u_2^2 + u_3^2\rangle}$, and the Taylor microscale is

$$\lambda = \sqrt{\frac{\langle u_1^2 + u_2^2 + u_3^2\rangle}{\langle(\partial u_1/\partial x_1)^2 + (\partial u_2/\partial x_2)^2 + (\partial u_3/\partial x_3)^2\rangle}}. \tag{9}$$

To evaluate the chemical reaction source, a Arrhenius-type single-step irreversible reaction equation is adopted [10,12]:

$$A + rB \rightarrow (1 + r)P, \tag{10}$$

where A and B denote two reactants, and P is the product. $r = 1$ is considered in the current study. The mass fractions and the reaction rates of species A, B, and P are represented by Y_A, Y_B, Y_P and $\dot{\omega}_A$, $\dot{\omega}_B$, $\dot{\omega}_P$, respectively. The thermodynamic properties of A, B, and P are assumed to be identical, and consequently, γ, C_p, C_v and the total molecular weight of the mixture W remain unchanged during the reaction process. The reaction rates of reactant and product are defined by [10,12]

$$\dot{\omega}_A = \dot{\omega}_B = -\tfrac{1}{2}\dot{\omega}_P = -\,\mathrm{Da}\,\rho^2 Y_A Y_B \exp(-\mathrm{Ze}/T), \tag{11}$$

where the Damköhler number $\mathrm{Da} = K_f \rho_f L_f/(U_f W_f^2)$ and the Zeldovich number $\mathrm{Ze} = E_a/RT_f$. K_f is the reaction rate parameter, which is assumed constant, and E_a is the activation energy [10,12].

The heat source term Q is defined by [10,12]

$$Q = \frac{\mathrm{Ce}}{(\gamma - 1)M^2}\dot{\omega}_P, \tag{12}$$

where the heat release parameter $\mathrm{Ce} = -H^0/C_pT_f$ and $-H^0$ is the heat of reaction [10,12]. The detailed derivation of dimensionless Navier-Stokes equations and the chemical reaction terms are referred to Appendix A.

It can be noted that the species production rate is determined by Da and Ze. The above two parameters in combination with Ce determine the heat generation rate. A statistically steady nonreacting compressible turbulence is used as initial conditions for velocity and temperature. The initial density field has a unity mean value and no turbulent fluctuations as shown in Fig. 1. In the x_1–x_3 planes, the initial mass fraction values of Y_A and Y_B are constant. The domain in the x_2

direction is uniformly divided into eight segments: $Y_A = 0.99$, $Y_B = 0.01$ in the first, third, fifth, and seventh segments, and $Y_A = 0.01$, $Y_B = 0.99$ in the second, fourth, sixth, and eighth segments. The spatial average of both Y_A and Y_B is equal to 0.5 and Y_P is zero over the entire domain. Details of the scalar initialization are given in Ref. [9]. It should be noted that Jaberi and Livescu *et al.* used random scalar initialization with a double-delta PDF distribution [5,10] and scalar slab initialization [12] in simulating a nonpremixed compressible isotropic, decaying, and shear reacting turbulence and found that when the simulation time is long enough, the conserved scalar variance is small. The influence of initial density fields on flow statistics is analyzed in Appendix B.

The governing equations of chemically reacting compressible turbulence are solved in conservative form in a cubic domain of $(2\pi)^3$ by using periodic boundary conditions in all three spatial directions. The time marching is performed by an explicit low storage second-order Runge-Kutta technique [33,34]. A hybrid scheme combining an eighth-order compact finite difference scheme [35] for smooth regions and a seventh-order weighted essentially nonoscillatory scheme [36] for shock regions [23,29,37] is adapted for moderately and highly compressible turbulence cases where $M_t \geqslant 0.4$. An eighth-order central compact finite difference scheme is applied for weakly compressible turbulence [35]. Successful applications of this numerical scheme are given in Wang *et al.* [32,38–42].

III. FLOW STATISTICS AND REACTION CHARACTERISTICS

Three sets of reaction parameters are employed to represent different reaction rates and heat release rates. The set $(\mathrm{Da} = 2,\ \mathrm{Ze} = 0, \mathrm{Ce} = 0)$ defines an isothermal reaction with only species production. The other two sets $(\mathrm{Da} = 200,\ \mathrm{Ze} = 8,\ \mathrm{Ce} = 3.168)$ and $(\mathrm{Da} = 3000,\ \mathrm{Ze} = 8,\ \mathrm{Ce} = 1.584)$ represent the exothermal reaction with different mass production rates and heat release rates. The zero-dimensional reaction is modeled according to Eqs. (13)–(15) for pure chemical reaction process analysis [4,10,12]. For the zero-dimensional model, the initial values of ρ, T, Y_A, and Y_B are 1.0, 1.0, 0.5, and 0.5, respectively. $\dot{\omega}_s$ and Q are calculated with Eq. (11) and Eq. (12), respectively:

$$\frac{d\rho}{dt} = 0, \tag{13}$$

$$\frac{dT}{dt} = \frac{\gamma \mathrm{Ce}}{\rho}\dot{\omega}_P, \tag{14}$$

$$\frac{dY_s}{dt} = \frac{\dot{\omega}_s}{\rho},\ \ s = A, B. \tag{15}$$

In DNSs, the specification of simulated parameters and resulting flow statistics are listed in Table I. Two sets of grid resolutions (128^3, 256^3) are employed for numerical simulations at initial Taylor Reynolds numbers 64 and 128, respectively. The turbulent Mach numbers are from 0.1 to 1.0. The Kolmogorov length scale is defined by $\eta = [\langle \mu/(\mathrm{Re}\,\rho)\rangle^3/\epsilon]^{1/4}$, where the dissipation rate per unit mass is given by $\epsilon = \langle \sigma_{ij} S_{ij}/(\mathrm{Re}\,\rho)\rangle$ and the strain rate tensor S_{ij} is defined by $S_{ij} = \frac{1}{2}(\frac{\partial u_i}{\partial x_j} + \frac{\partial u_j}{\partial x_i})$. The magnitude of the Kolmogorov length scale η represents the dissipation-range resolution, which plays a significant role in the grid convergence of velocity statistics in DNS [43]. As shown in the table, the resolution parameter $\eta/\Delta x$ lies within the range between 0.97 and 1.06, where Δx denotes the grid length in each direction. It is straightforward to derive that $3.05 < k_{\max}\eta < 3.33$ where the largest wave number $k_{\max}$ is half of the number of grids N in each direction: $k_{\max} = N/2 = \pi/\Delta x$. Previous DNS results [28] showed that the resolution parameter $\eta/\Delta x \geqslant 0.5$ is enough for convergence of high-order moments of velocity gradients. For a high turbulent Mach number $M_t \geqslant 0.5$, the resolution parameter $\eta/\Delta x > 0.98$. Therefore, the overall statistics should be well converged in current numerical simulations.

TABLE I. Specification of DNS parameters and resulting flow statistics.

Resolution	Re_λ	M_t	Da	Ze	Ce	$\eta/\Delta x$	L_I/η	λ/η	S_3
128^3	62.15	0.09	2	0	0	1.01	34.02	15.80	−0.44
128^3	63.61	0.19	2	0	0	0.99	34.54	16.10	−0.41
128^3	63.58	0.37	2	0	0	1.01	34.07	16.03	−0.42
128^3	63.65	0.55	2	0	0	1.03	33.63	15.89	−0.47
128^3	62.04	0.73	2	0	0	1.05	33.33	15.24	−0.66
128^3	61.46	0.92	2	0	0	1.06	33.22	14.99	−1.14
128^3	62.52	0.09	200	8	3.168	1.00	34.11	15.92	−0.40
128^3	62.50	0.19	200	8	3.168	0.99	34.60	15.86	−0.40
128^3	61.50	0.37	200	8	3.168	1.01	34.12	15.54	−0.43
128^3	56.13	0.55	200	8	3.168	1.03	34.02	14.06	−1.65
128^3	54.38	0.74	200	8	3.168	1.04	33.73	13.25	−1.98
128^3	62.48	0.09	3000	8	1.584	1.02	34.14	15.83	−0.40
128^3	62.58	0.19	3000	8	1.584	1.00	34.29	15.72	−0.39
128^3	61.50	0.37	3000	8	1.584	1.01	34.12	15.54	−0.43
128^3	54.69	0.55	3000	8	1.584	1.02	34.29	13.62	−1.67
256^3	99.35	0.10	2	0	0	0.98	62.54	19.79	−0.46
256^3	98.99	0.20	2	0	0	0.97	62.76	19.70	−0.47
256^3	102.74	0.40	2	0	0	0.98	63.03	20.12	−0.46
256^3	102.57	0.60	2	0	0	0.98	62.83	19.88	−0.46
256^3	100.30	0.80	2	0	0	0.99	62.53	19.09	−0.80
256^3	99.33	0.99	2	0	0	1.03	61.85	18.39	−1.50
256^3	100.01	0.10	200	8	3.168	0.98	62.51	19.85	−0.46
256^3	99.82	0.20	200	8	3.168	0.98	62.68	19.74	−0.46
256^3	97.63	0.40	200	8	3.168	0.98	63.13	19.12	−0.70
256^3	93.67	0.60	200	8	3.168	0.99	62.97	18.04	−1.47
256^3	91.78	0.80	200	8	3.168	1.01	62.06	17.23	−1.98
256^3	99.95	0.10	3000	8	1.584	0.98	62.61	19.83	−0.45
256^3	99.18	0.20	3000	8	1.584	1.01	61.93	19.26	−0.59
256^3	93.59	0.39	3000	8	1.584	1.00	62.85	18.14	−1.54
256^3	92.50	0.59	3000	8	1.584	1.00	62.95	17.73	−2.06

The integral length scale L_I is defined by [29]

$$L_I = \frac{3\pi}{2(u')^2} \int_0^\infty \frac{E^u(k)}{k}\, dk, \tag{16}$$

where $E^u(k)$ is the spectrum of kinetic energy per unit mass, namely, $\int_0^\infty E^u(k)\, dk = (u')^2/2$. The ratio of L_I/η lies within the range $33 \leqslant L_I/\eta \leqslant 63$ in current simulation cases.

The velocity derivative skewness S_3 is defined by

$$S_3 = \frac{[\langle(\partial u_1/\partial x_1)^3 + (\partial u_2/\partial x_2)^3 + (\partial u_3/\partial x_3)^3\rangle]/3}{\{\langle(\partial u_1/\partial x_1)^2 + (\partial u_2/\partial x_2)^2 + (\partial u_3/\partial x_3)^2\rangle/3\}^{3/2}}. \tag{17}$$

In isothermal reaction cases ($\mathrm{Da} = 2$) at small turbulent Mach numbers $M_t \leqslant 0.6$, values of S_3 are similar to typical values of -0.6 to -0.4 in nonreacting weakly compressible turbulence [28]. As turbulent Mach number increases, the formation of shocklets in compressible turbulence results in a larger magnitude of S_3. The magnitude of S_3 is significantly enhanced in the situations of exothermal reactions ($\mathrm{Da} = 200, 3000$) at $M_t \geqslant 0.55$, due to the increase of compressibility induced by reaction heat release.

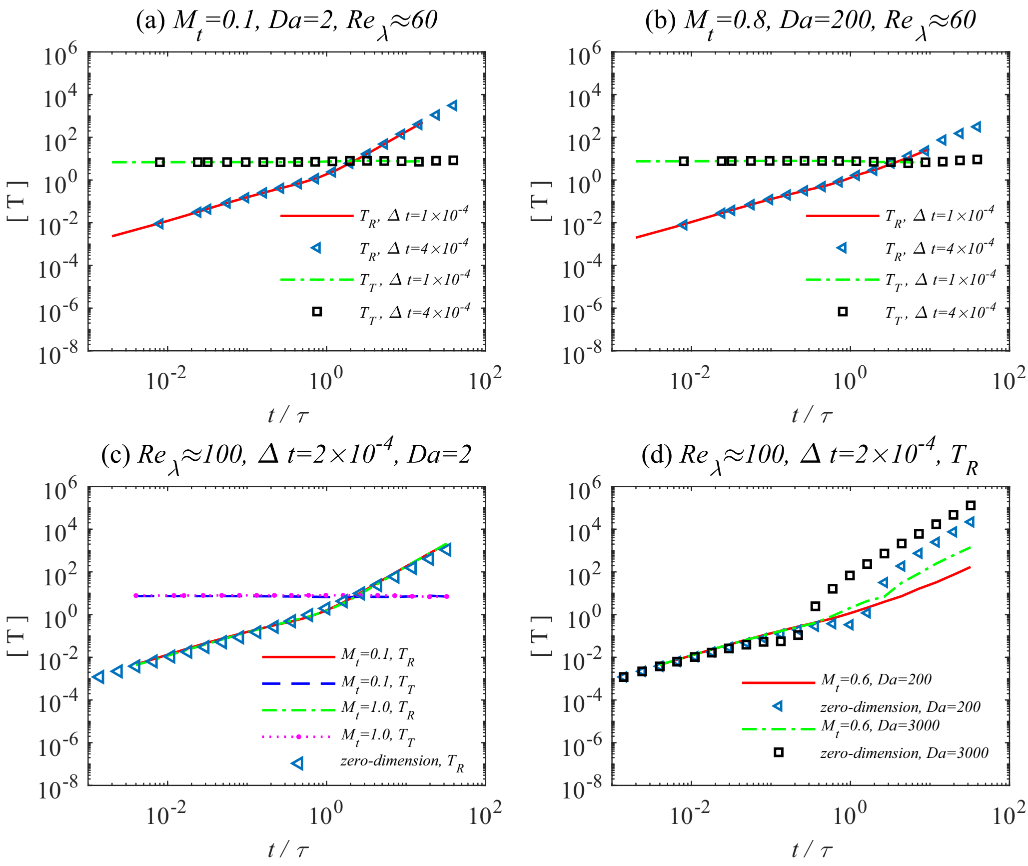

FIG. 2. Temporal variation of turbulent timescale T_T and reaction timescale T_R (a) at $M_t = 0.1$ in isothermal reactions ($\mathrm{Da} = 2$) for $\mathrm{Re}_\lambda \approx 60$, (b) at $M_t = 0.8$ in exothermal reactions ($\mathrm{Da} = 200$) for $\mathrm{Re}_\lambda \approx 60$, (c) at $M_t = 0.1$ and 1.0 in isothermal reactions ($\mathrm{Da} = 2$) for $\mathrm{Re}_\lambda \approx 100$, and (d) at $M_t = 0.6$ in exothermal reactions ($\mathrm{Da} = 200$, 3000) for $\mathrm{Re}_\lambda \approx 100$.

The characteristic reaction time $T_R = \rho Y_P/\dot{\omega}_P$ and turbulent time $T_T = 2K/\epsilon$ are used to evaluate the timescales during the reaction process where $K = \langle[(u_1)^2 + (u_2)^2 + (u_3)^2]/2\rangle$ is the kinetic energy per unit mass. The simulation time t is nondimensionalized by the large-eddy turnover time $\tau = L_I/u'$. Three time steps of numerical integration ($\Delta t = 1 \times 10^{-4}$, 2×10^{-4}, and 4×10^{-4}) are used to validate the temporal resolution of the current adopted time step ($\Delta t = 2 \times 10^{-4}$) for turbulent motion and the chemical reaction. Figure 2(a) shows T_R and T_T at $M_t = 0.1$ under the isothermal reaction ($\mathrm{Da} = 2$) at Taylor Reynolds number $\mathrm{Re}_\lambda \approx 60$ ($\Delta t = 2 \times 10^{-4}$ data are not plotted in the figure). It is shown that during the reaction process, turbulent time T_T maintains a quasiconstant value while the reaction time increases with the increase of t/τ. The two timescales coincide with each other approximately at $t/\tau = 1.7$. For both the reaction time and turbulent time, the data collapse with each other for the different time steps. For exothermal reaction cases ($\mathrm{Da} = 200$) at $M_t = 0.8$ shown in Fig. 2(b) ($\Delta t = 2 \times 10^{-4}$ data are not plotted in the figure), the characteristic time variation behavior is similar to that in the case $\mathrm{Da} = 2$. The two characteristic times coincide with each other approximately at $t/\tau = 3.3$. The results shown in Figs. 2(a) and 2(b) suggest that the current adopted time step ($\Delta t = 2 \times 10^{-4}$) can well resolve both turbulent motion and the chemical reaction. Figure 2(c) compares T_R and T_T at $M_t = 0.1$ and 1.0 under the isothermal reaction ($\mathrm{Da} = 2$) at Taylor Reynolds number $\mathrm{Re}_\lambda \approx 100$. The match of characteristic time at

$M_t = 0.1$ and 1.0 suggests that the turbulent Mach number has little influence on both turbulent and reaction timescales. The reaction time can be well predicted by the zero-dimensional model in isothermal reaction cases. Figure 2(d) plots the reaction time at $M_t = 0.6$ for two exothermal reactions ($\mathrm{Da} = 200, 3000$) at Taylor Reynolds number $\mathrm{Re}_\lambda \approx 100$. It is shown that T_R collapse with each other for the two exothermal reactions at $t/\tau < 0.3$. The reaction time can be well predicted by the zero-dimensional model at $t/\tau < 0.08$. When $t/\tau > 0.08$, the zero-dimensional model overpredicts the reaction time. It suggests that in exothermal reactions, the reaction time is dependent of the inherent reaction features as well as turbulent motion.

Figure 3 plots temporal variation of the mass fraction of different species at different turbulent Mach numbers, Taylor Reynolds numbers, and reaction parameters. The nondimensional time $t/\tau = 0$ denotes the start of species mixing and the chemical reaction while simulations end at $t/\tau = 34$ corresponding to approximately 95% reactant consumption. Figures 3(a)–3(d) show the influence of the turbulent Mach number on product generation rates in both isothermal ($\mathrm{Da} = 2$) and exothermal reactions ($\mathrm{Da} = 200$). Data used in Figs. 3(a), 3(c), and 3(e) are identical with data in Figs. 3(b), 3(d), and 3(f) respectively. As shown in Fig. 3(a), the mass fraction of product P increases rapidly at $t/\tau = 0$–0.8. Figure 3(b) shows that the overall product mass fractions grow rapidly from $t/\tau = 0$ to 4. The overlap of curves at turbulent Mach number $M_t = 0.1$–1.0 suggests that the temporal variation of species mass fraction in isothermal reactions is not affected by M_t. In exothermal reactions shown in Fig. 3(c), the growth rate of the product mass fraction also increases rapidly at $t/\tau = 0$–0.8. An increase of the turbulent Mach number can accelerate product generation for $t/\tau > 0.8$ as shown in Fig. 3(d). For $M_t = 0.1$ and 0.4, the two curves are very close to each other, indicating that for weakly compressible turbulence where $M_t \leqslant 0.4$, the turbulent Mach number has a limited influence on the product generation rate. Figures 3(e) and 3(f) plot the temporal variation of reactant and product mass fraction in exothermal reaction ($\mathrm{Da} = 3000$) at $M_t = 0.6$ and $\mathrm{Re}_\lambda \approx 60{,}100$ respectively. Symbols represent zero-dimensional model solutions under the same reaction parameters without turbulent motion. It is shown that the Reynolds number basically has a minor influence on both reactant consumption and the product generation rate. At $t/\tau \leqslant 0.1$, the temporal variation of reactant A collapses with the zero-dimensional model solution, indicating that turbulent motion has little influence on reactant consumption at the initial phrase of the reaction in turbulence. However, the product generation rate from simulations deviates from the zero-dimensional model growth rate for product mass fraction, suggesting that advection and diffusion can effectively influence product generation rate during this period. At $t/\tau > 0.1$, the reactant consumes faster in the zero-dimensional model than the actual consumption rate in simulations, indicating that turbulent motion has an effect to slow chemical reactions due to advection and diffusion.

Temporal variation of reaction rate W for isothermal ($\mathrm{Da} = 2$) and exothermal ($\mathrm{Da} = 200$) reactions at different turbulent Mach numbers are shown in Figs. 4(a)–4(d), where $W = -\dot{\omega}_A = \mathrm{Da}\, \rho^2 Y_A Y_B \exp(-\mathrm{Ze}/T)$. In general, the reaction rate for both reaction parameters exhibits a rapid increase and then a subsequent decrease. For isothermal reaction cases shown in Figs. 4(a) and 4(b), the turbulent Mach number has only limited influence on the reaction rate at the very initial phrase from $t/\tau = 0$–1.7×10^{-2} and after that different curves of the reaction rate overlap with each other for $M_t = 0.1$–1.0. The zero-dimensional model results marked with "$\triangleleft$" coincide with numerical solutions only when $t/\tau > 8$. The inconsistency of the zero-dimensional model data for $t/\tau = 0$–0.8 results from omitting reactant advection and diffusion in the zero-dimensional model. The reaction rate W increases gradually for $t/\tau = 0$–0.8 in simulations while W holds nearly constant in the zero-dimensional model solution during this period. For exothermal reactions ($\mathrm{Da} = 200$) shown in Figs. 4(c) and 4(d), a high turbulent Mach number can effectively accelerate the reaction speed for $t/\tau > 0.8$. It can be noted that when $t/\tau > 15$, a high turbulent Mach number decreases the reaction rate due to the fast consumption of reactants during $t/\tau = 0.8$–15. Heat release enhances turbulent motion and induces the reaction rate fluctuation. Figures 4(e) and 4(f) show temporal variation of the mixing rate, which is defined as $G = \rho^2 Y_A Y_B$ for three reaction parameters ($\mathrm{Da} = 2, 200, 3000$) at $M_t = 0.6$. The mixing rate G increases gradually at $t/\tau = 0$–0.8

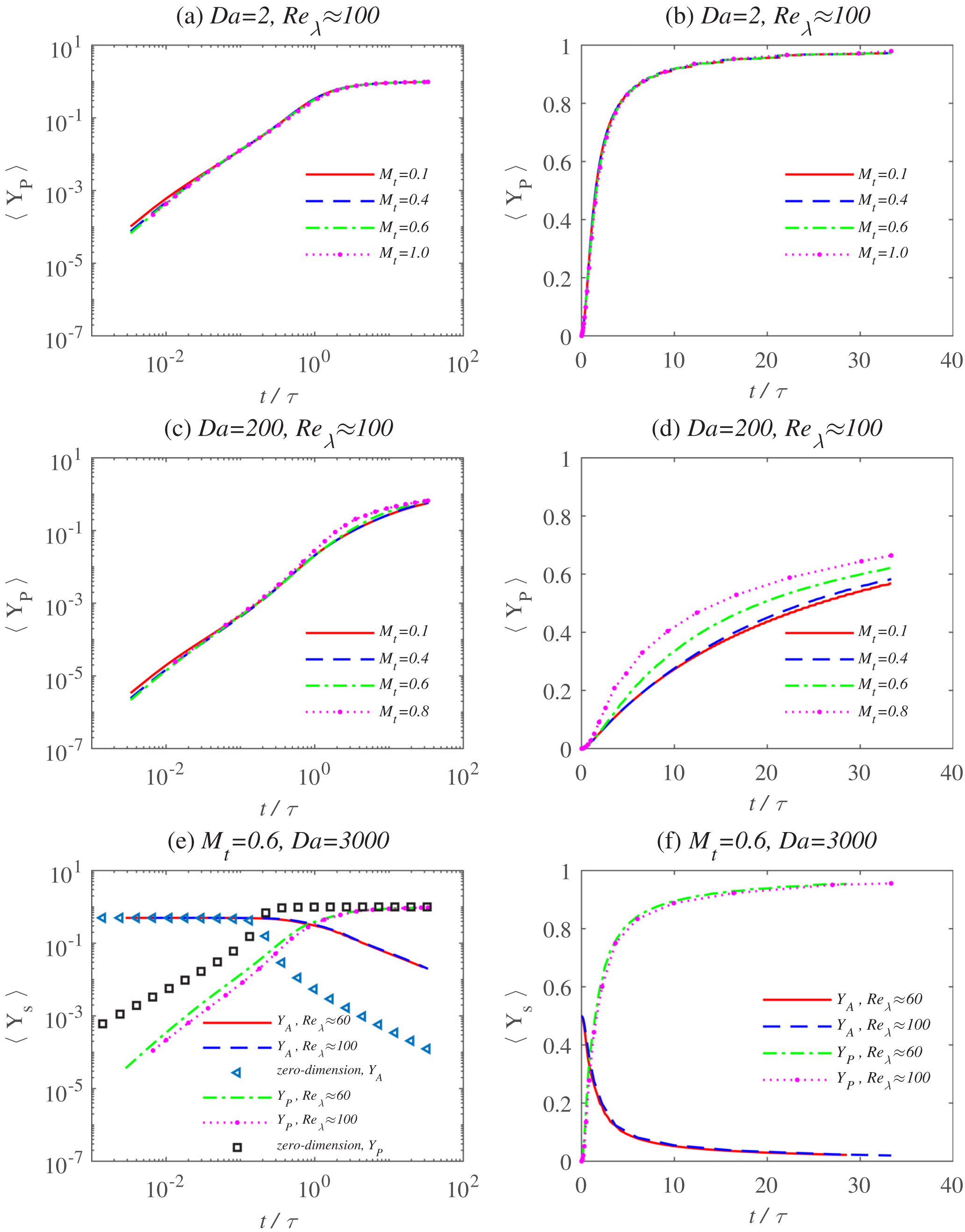

FIG. 3. Temporal variation of mass fraction of different species. (a, b) Product P at $M_t = 0.1$-1.0 in isothermal reactions ($\mathrm{Da} = 2$) at $\mathrm{Re}_\lambda \approx 100$, (c, d) product P at $M_t = 0.1$–0.8 in exothermal reactions ($\mathrm{Da} = 200$) at $\mathrm{Re}_\lambda \approx 100$, (e, f) reactant A and product P at $M_t = 0.6$ in exothermal reactions ($\mathrm{Da} = 3000$) at $\mathrm{Re}_\lambda \approx 60$ and $\mathrm{Re}_\lambda \approx 100$.

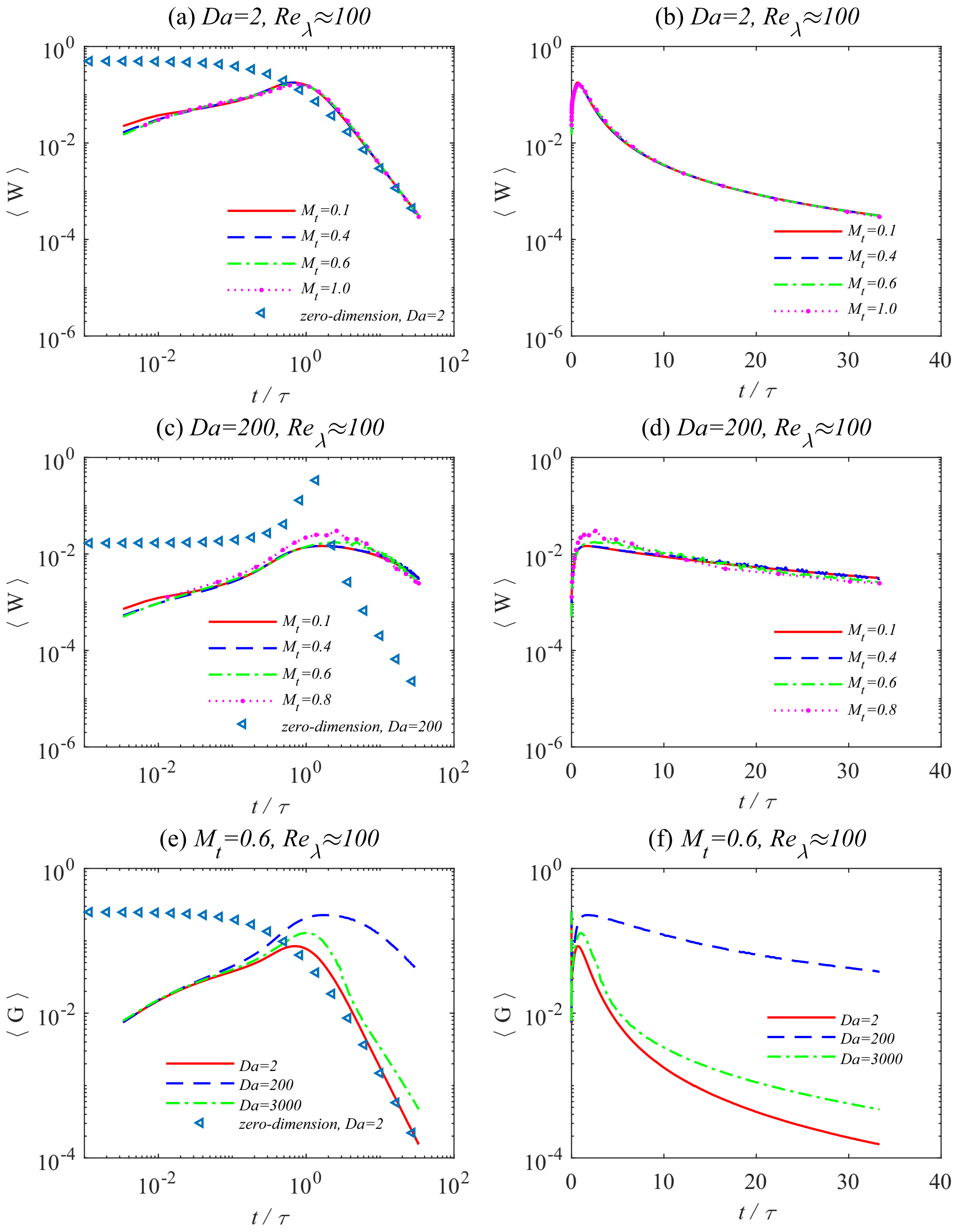

FIG. 4. Temporal variation of (a, b) reaction rate W at $M_t = 0.1$–1.0 in isothermal reactions (Da $= 2$) at $\mathrm{Re}_\lambda \approx 100$, (c, d) reaction rate W at $M_t = 0.1$–0.8 in exothermal reactions (Da $= 200$) at $\mathrm{Re}_\lambda \approx 100$, (e, f) mixing rate G at $M_t = 0.6$ in three reactions (Da $= 2$, 200, 3000) at $\mathrm{Re}_\lambda \approx 100$.

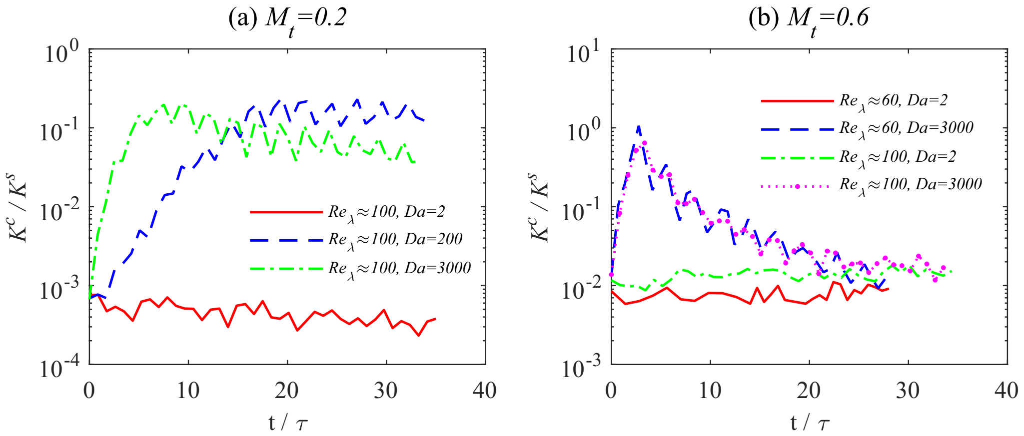

FIG. 5. Temporal variation of compressible to solenoidal kinetic energy ratio (a) at $M_t = 0.2$ in three reactions (Da = 2, 200, 3000) for $\mathrm{Re}_\lambda \approx 100$ and (b) at $M_t = 0.6$ in two reactions (Da = 2, 3000) for $\mathrm{Re}_\lambda \approx 60$ and $\mathrm{Re}_\lambda \approx 100$.

and then decreases at $t > 0.8$ for three reaction parameters. The zero-dimensional model results coincide with numerical solutions when $t/\tau > 6$. During most of the reaction period, the mixing rate in the case Da = 200 is apparently larger than the other two reaction groups (Da = 2, 3000).

The Helmholtz decomposition is applied to decompose the velocity field $\boldsymbol{u}$ into a solenoidal component $\boldsymbol{u}^s$ and a compressible component $\boldsymbol{u}^c$ [29]: $\boldsymbol{u} = \boldsymbol{u}^s + \boldsymbol{u}^c$, where $\nabla \cdot \boldsymbol{u}^s = 0$ and $\nabla \times \boldsymbol{u}^c = 0$. The two components of kinetic energy per unit mass can therefore be defined as $K^s = \langle [(u_1^s)^2 + (u_2^s)^2 + (u_3^s)^2]/2 \rangle$ and $K^c = \langle [(u_1^c)^2 + (u_2^c)^2 + (u_3^c)^2]/2 \rangle$, respectively. Follow the Helmholtz decomposition, the dissipation rate of kinetic energy per unit mass is given by $\epsilon = \epsilon^s + \epsilon^c$ where the solenoidal component is $\epsilon^s = \langle \mu/(\mathrm{Re}\,\rho) \rangle \langle \omega_i \omega_i \rangle$ and the compressible component is $\epsilon^c = \langle 4\mu/(3\,\mathrm{Re}\,\rho) \rangle \langle \theta^2 \rangle$ [23,44,45]. Figure 5 shows temporal variation of the ratio of compressible to solenoidal kinetic energy K^c/K^s in three reaction cases (Da = 2, 200, 300) at turbulent Mach numbers $M_t = 0.2$ and 0.6. Figure 5(a) shows that at $M_t = 0.2$ and Taylor Reynolds number $\mathrm{Re}_\lambda \approx 100$, the kinetic energy ratio in both exothermal reactions (Da = 200, 3000) dramatically increases approximately from 10^{-3} to 10^{-1} at $t/\tau = 0$–21. Paes [6] indicated that strong heat release promotes pressure dilatation work, leading to an increase in turbulent kinetic energy. In the isothermal reaction case Da = 2, the kinetic energy ratio retains almost constant with a slight decrease during the entire reaction process. The kinetic energy ratio in all three reaction cases reaches a nearly equilibrium state when $t/\tau > 21$. Figure 5(b) shows the ratio of compressible kinetic energy to solenoidal kinetic energy at different Taylor Reynolds number for $M_t = 0.6$. It is shown that the kinetic energy ratio at both $\mathrm{Re}_\lambda \approx 60$ and $\mathrm{Re}_\lambda \approx 100$ in exothermal cases (Da = 3000) experiences a sudden increase for $0 < t/\tau < 4$ and then decreases gradually. The effect of the Taylor Reynolds number on the kinetic energy ratio is very small in both isothermal and exothermal reactions.

Figure 6 shows temporal variation of the ratio of the compressible component to solenoidal component of kinetic energy dissipation ϵ^c/ϵ^s in three reaction cases (Da = 2, 200, 300) at turbulent Mach number $M_t = 0.2$ and 0.6. In exothermal reactions (Da = 200, 3000) as shown in Fig. 6(a), the increase of the magnitude of velocity divergence by heat release leads to a corresponding increase in kinetic energy dissipation rate [6]. The influence of the Taylor Reynolds number on the dissipation ratio is small as shown in Fig. 6(b). Figures 5 and 6 demonstrate that when $t/\tau > 25$ in both low and high turbulent Mach number cases, the flow is nearly statistically steady.

Figure 7 shows isosurfaces of the instantaneous reaction rate W and velocity divergence θ from $M_t = 0.2$ to 0.8 under exothermal reactions (Da = 200). At $M_t = 0.2$, the isosurfaces of velocity

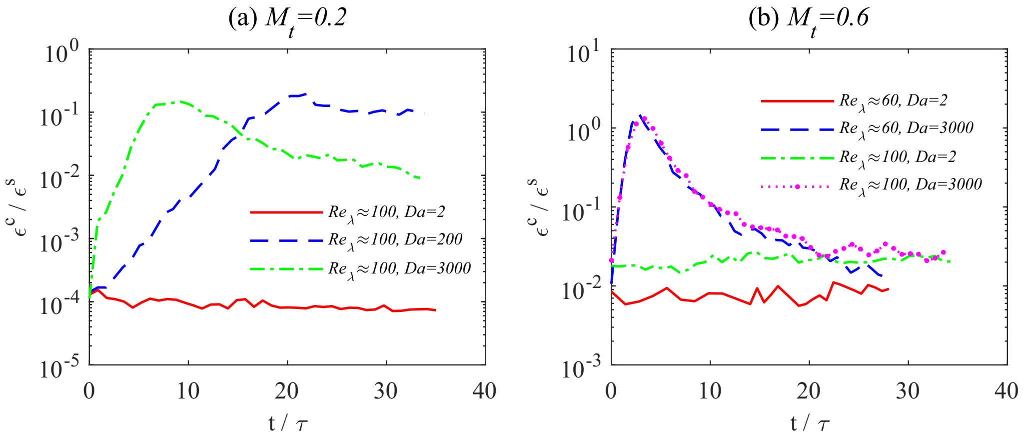

FIG. 6. Temporal variation of compressible to solenoidal dissipation rate ratio (a) at $M_t = 0.2$ in three reactions (Da = 2, 200, 3000) at $\mathrm{Re}_\lambda \approx 100$ and (b) at $M_t = 0.6$ in two reactions (Da = 2, 3000) at $\mathrm{Re}_\lambda \approx 60$ and $\mathrm{Re}_\lambda \approx 100$.

divergence exhibit bloblike shapes. As M_t increases from $M_t = 0.2$, to $M_t = 0.4$ and 0.6, isosurfaces of velocity divergence become sheetlike due to the generation of shocklets [29,46]. When M_t further increases to 0.8, the length scales of sheetlike isosurfaces of velocity divergence become larger due stronger shocklets being generated at a higher turbulent Mach number [23]. The isosurfaces of the reaction rate retain sheetlike structures from low to high turbulent Mach number cases. As M_t increases, the strong turbulent compression leads to an increase of the reaction rate surface area. It is also observed that the sheetlike structures of reaction rate isosurfaces are not correlated with the velocity divergence isosurface structures. This observation can be interpreted as follows. Internal energy increased by the chemical heat release can be converted to compressible part of kinetic energy through pressure work [4]. The increased compressible kinetic energy leads to an enhanced compression motion [4]. The correlation between reaction rate and velocity divergence is weak because the overall processes of energy transfer and the formation of strong compression structures (negative velocity divergence isosurfaces) are quite slow compared to the timescale of reaction.

IV. SPECTRA OF VELOCITY AND THERMODYNAMIC VARIABLES

A. Spectra of velocity and its compressible component

Before the discussion of the spectra of velocity and its compressible component, the statistics of the local reaction rate W are presented. Figure 8 shows the temporal evolution of the probability density function (PDF) of reaction rate W for isothermal (Da = 2) and exothermal (Da = 200) reactions at turbulent Mach numbers $M_t = 0.2$ and 0.8 and at $\mathrm{Re}_\lambda \approx 100$. It can be found that for isothermal (Da = 2) and exothermal (Da = 200) reactions at $M_t = 0.1$ as shown in Figs. 8(a) and 8(b), the left tails of PDFs are longer than their right tails at $t/\tau = 0.9$. With the increase of time, the peaks of PDFs decrease for both isothermal and exothermal reactions, and the PDFs become nearly symmetric when $t/\tau > 0.9$. It can be observed that the two tails of PDFs become shorter as reaction proceeds, which indicate that the spatial fluctuations of local reaction rate W become smaller. At $M_t = 0.8$ as shown in Figs. 8(c) and 8(d), the right tails of PDFs are longer than their left tails, and the right tails of the PDFs become shorter as the reaction proceeds. It is found that the reaction rate W becomes smaller with the increase of time for isothermal (Da = 2) and exothermal (Da = 200) reactions at $M_t = 0.8$ during the reaction process.

Figure 9 shows temporal evolution of the compensated spectrum of velocity $E^u(k)\epsilon^{-2/3}k^{5/3}$ for isothermal reaction (Da = 2) and exothermal reaction (Da = 200) cases at turbulent Mach number

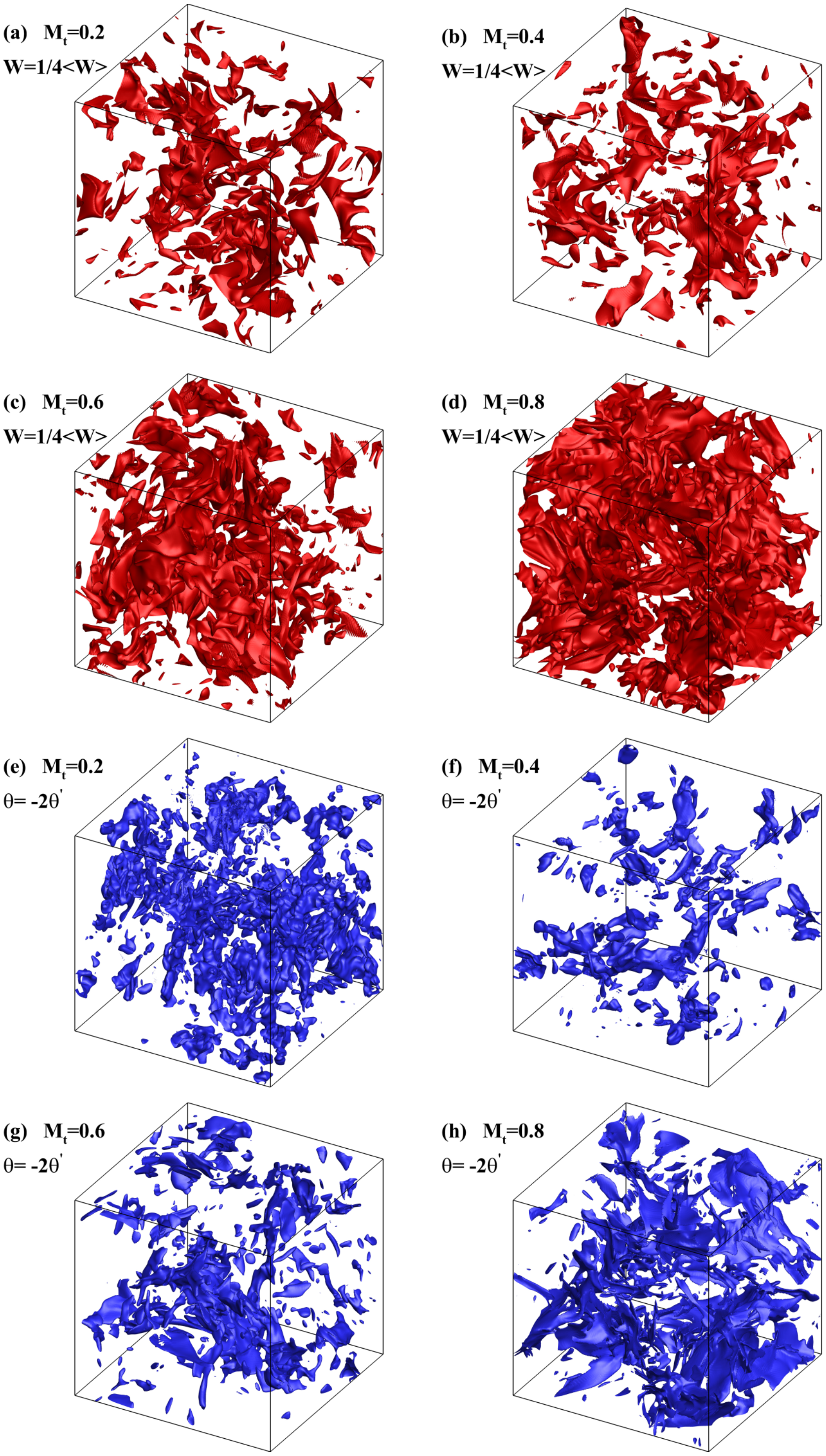

FIG. 7. Isosurfaces of instantaneous reaction rate (red, $W = \frac{1}{4}\langle W \rangle$) and velocity divergence (blue, $\theta = -2\theta'$) isosurfaces with 256^3 grid resolution in exothermal reactions (Da = 200) for $t/\tau = 0.8$ at $\mathrm{Re}_\lambda \approx 100$ and different turbulent Mach numbers: (a, e) $M_t = 0.2$; (b, f) $M_t = 0.4$; (c, g) $M_t = 0.6$; (d, h) $M_t = 0.8$.

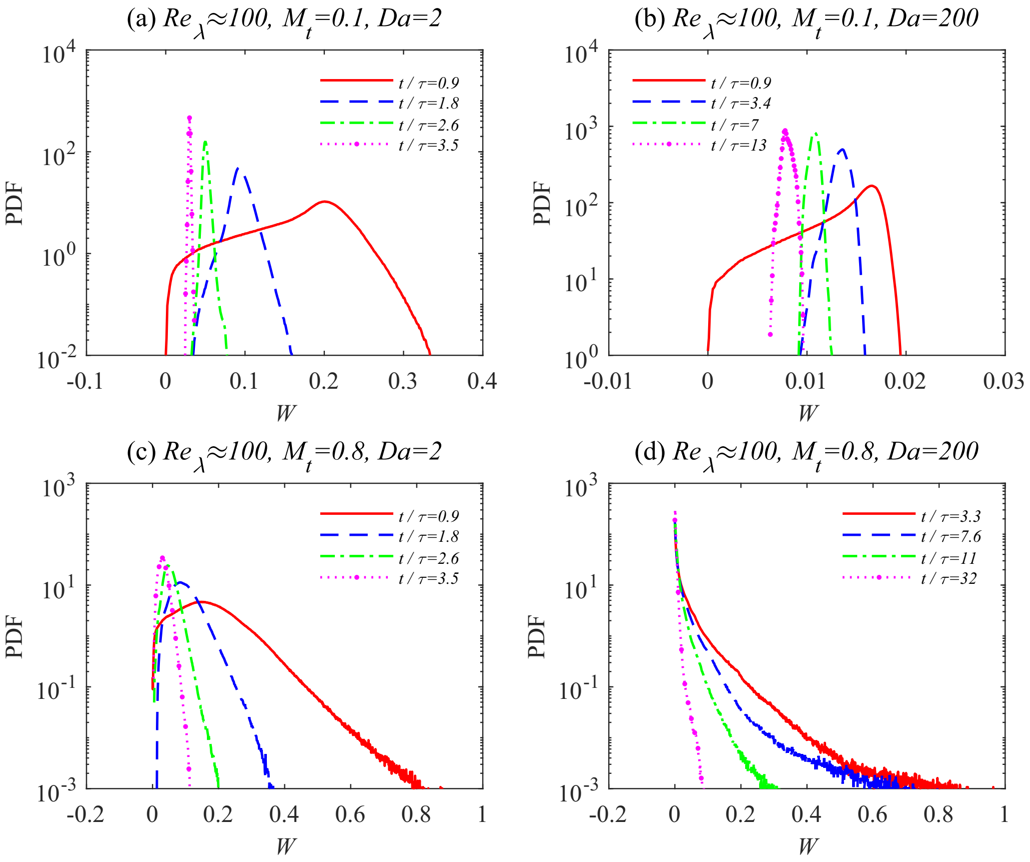

FIG. 8. PDF of reaction rate W at Taylor Reynolds number $\mathrm{Re}_\lambda \approx 100$. (a) $M_t = 0.1$, $\mathrm{Da} = 2$; (b) $M_t = 0.1$, $\mathrm{Da} = 200$; (c) $M_t = 0.8$, $\mathrm{Da} = 2$; (d) $M_t = 0.8$, $\mathrm{Da} = 200$.

$M_t = 0.2$, 0.8 and at Taylor Reynolds number $\mathrm{Re}_\lambda \approx 100$. At $M_t = 0.2$ in the isothermal reaction ($\mathrm{Da} = 2$) shown in Fig. 9(a), the compensated velocity spectrum maintains a statistically steady state where the spectral distribution spans approximately identically along with time. In the exothermal reaction ($\mathrm{Da} = 200$) shown in Fig. 9(b), due to the effect of heat release, the spectrum at $k\eta \geqslant 1$ is gradually elevated, while at a low $k\eta$ value, the spectral distribution remains unchanged similar to the initial value. At a high turbulent Mach number $M_t = 0.8$ in the isothermal reaction ($\mathrm{Da} = 2$) shown in Fig. 9(c), the spectrum remains unchanged during the reaction process similar to the low turbulent Mach number case ($M_t = 0.2$). However, in the exothermal reaction ($\mathrm{Da} = 200$) shown in Fig. 9(d), the spectrum is elevated in the scale range $k\eta \geqslant 0.01$. At $t/\tau = 4$ corresponding to the time of the maximum reaction rate shown in Fig. 4(c), the compensated spectrum of velocity also reaches a summit and then gradually decreases when $t/\tau > 17$. In exothermal reactions at turbulent Mach number $M_t = 0.2$ and 0.8, the chemical reaction heat release mainly affects the compensated spectrum of velocity in the high $k\eta$ range.

The instantaneous compensated spectrum of velocity $E^u(k)\epsilon^{-2/3}k^{5/3}$ at the turbulent Mach number $M_t = 0.1$–0.8 and at Taylor Reynolds number $\mathrm{Re}_\lambda \approx 100$ for three reaction parameters ($\mathrm{Da} = 2$, 200, 3000) is plotted in Fig. 10. Figure 10(a) shows the effect of turbulent Mach number on the compensated velocity spectrum in exothermal reactions ($\mathrm{Da} = 200$). The inertial range of velocity spectra can be identified through $E^u(k)\epsilon^{-2/3}k^{5/3} \approx C_K$, where the Kolmogorov constant $C_K = 1.6$, which is close to typical values of 1.5 to 2.0 observed in nonreacting homogeneous

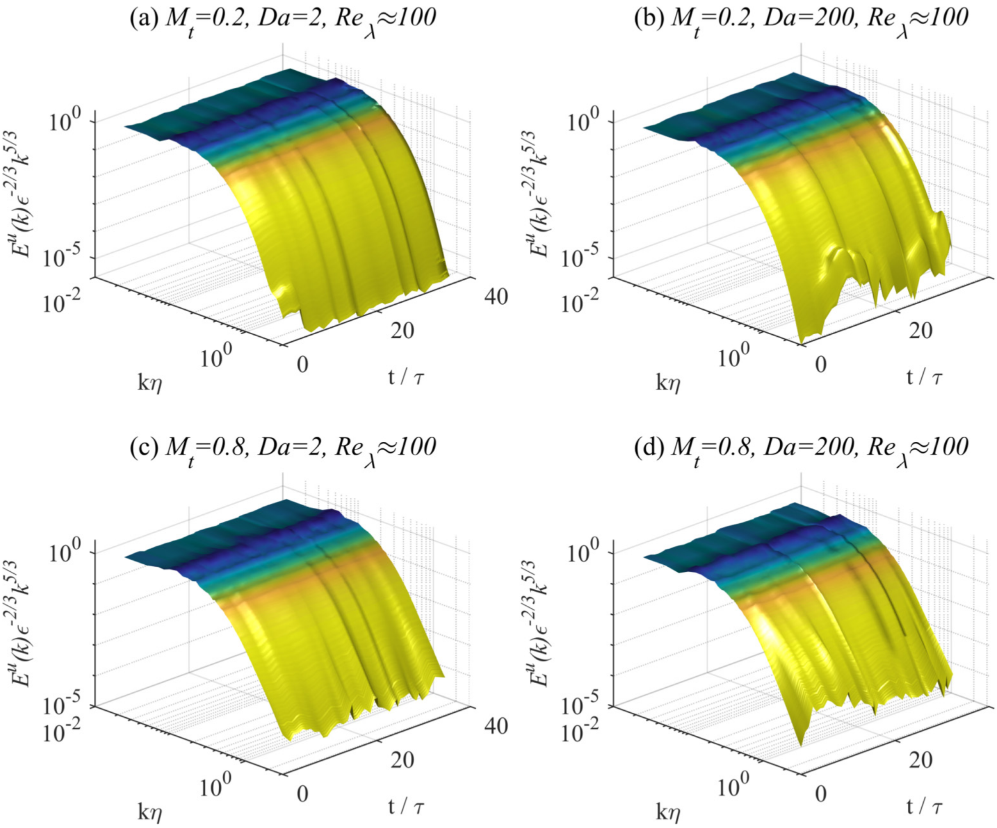

FIG. 9. Temporal variation of compensated spectrum of velocity $E^u(k)\epsilon^{-2/3}k^{5/3}$ for isothermal and exothermal reactions at Taylor Reynolds number $\mathrm{Re}_\lambda \approx 100$. (a) $M_t = 0.2$, $\mathrm{Da} = 2$; (b) $M_t = 0.2$, $\mathrm{Da} = 200$; (c) $M_t = 0.8$, $\mathrm{Da} = 2$; (d) $M_t = 0.8$, $\mathrm{Da} = 200$.

isotropic turbulence [28]. The compensated spectra of velocity $E^u(k)\epsilon^{-2/3}k^{5/3}$ nearly overlap with each other for $k\eta < 1$. However, for $k\eta \geqslant 1$, the heat release leads to the increase of the velocity spectrum. The temporal evolution of the compensated spectrum of velocity in an exothermal reaction ($\mathrm{Da} = 200$) at $M_t = 0.1$ is plotted in Fig. 10(b). The spectrum remains unaffected at $k\eta < 1$ throughout the reaction process. At $k\eta \geqslant 1$, the spectrum gradually increases with the increase of time. At $t/\tau = 34$, the spectrum becomes larger than 10^{-2} for $k\eta \geqslant 1$. At turbulent Mach number $M_t = 0.6$ in the exothermal reaction ($\mathrm{Da} = 3000$) shown in Fig. 10(c), the impact of the reaction heat release on compensated spectrum of velocity is significant at $k\eta \geqslant 1$ in the middle stage of the reaction process ($t/\tau = 2.5$–7). At the end of the simulation, the spectrum nearly overlaps with the initial value, indicating that heat-release-induced velocity fluctuation can be quickly dissipated when the heat release rate becomes weak. Figure 10(d) shows the effect of the heat release rate on the compensated spectrum of velocity at $M_t = 0.6$. The compensated spectrum of velocity $E^u(k)\epsilon^{-2/3}k^{5/3}$ at three reaction parameters over the entire wave number range collapse with each other at the end of simulations, which is very close to the initial value of the compensated velocity spectrum.

Figure 11 shows the temporal evolution of the compensated spectrum of compressible velocity component $E^{u,C}(k)\epsilon^{-2/3}k^{5/3}$ for exothermal reactions ($\mathrm{Da} = 200$) at Taylor Reynolds number $\mathrm{Re}_\lambda \approx 100$ and at turbulent Mach number $M_t = 0.2$–0.8. The spectrum of the compressible velocity $E^{u,C}(k)$ satisfies $\int_0^\infty E^{u,C}(k)\,dk = \langle (\boldsymbol{u}^C)^2/2\rangle$. As shown in Fig. 11(a), at turbulent Mach number

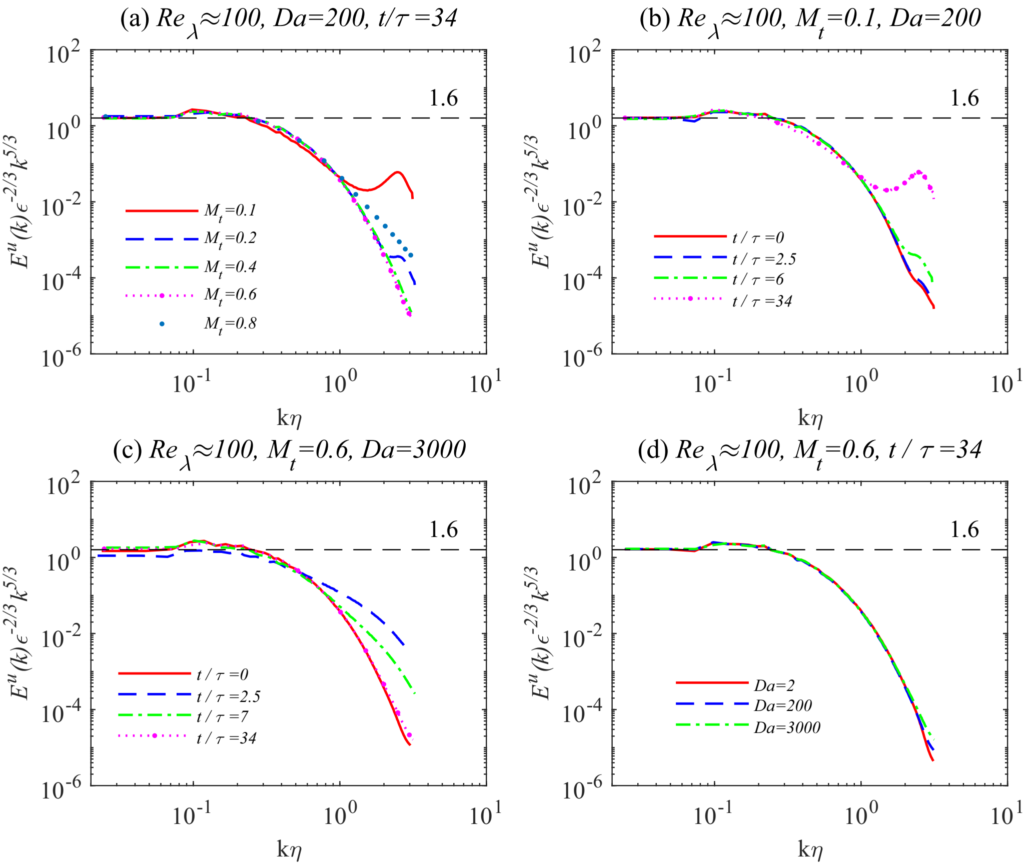

FIG. 10. Instantaneous compensated spectrum of velocity $E^u(k)\epsilon^{-2/3}k^{5/3}$ at Taylor Reynolds number $\mathrm{Re}_\lambda \approx 100$ for three reaction parameters. (a) $M_t = 0.1$–0.8, $\mathrm{Da} = 200$, $t/\tau = 34$; (b) $M_t = 0.1$, $\mathrm{Da} = 200$, $t/\tau = 0$–34; (c) $M_t = 0.6$, $\mathrm{Da} = 3000$, $t/\tau = 0$–34; (d) $M_t = 0.6$, $\mathrm{Da} = 2, 200, 3000$, $t/\tau = 34$.

$M_t = 0.2$ during $t/\tau = 0$–17, the spectrum gradually increases over the entire wave number range. When $t/\tau > 20$, the spectrum reaches a nearly steady state and is comparably larger than the initial value over the entire wave number range. At $M_t = 0.4$ shown in Fig. 11(b), the temporal variation of the compensated spectrum of the compressible velocity component is similar to the $M_t = 0.2$ case. At high turbulent Mach numbers $M_t = 0.6$ and $M_t = 0.8$ shown in Figs. 11(c) and 11(d), respectively, the spectra are elevated over the entire wave number range at $t/\tau = 0$–8. The increase of the turbulent Mach number for exothermal reactions can suppress the spectrum increase at the intermediate and high wave number range and also decrease the overall spectrum elevation extent.

The instantaneous compensated spectrum of the compressible velocity component $E^{u,C}(k)\epsilon^{-2/3}k^{5/3}$ at $M_t = 0.1$–0.8 and $\mathrm{Re}_\lambda \approx 100$ for three reaction parameters ($\mathrm{Da} = 2, 200, 3000$) is shown in Fig. 12. Figure 12(a) shows the effect of the turbulent Mach number on the compensated spectrum of the compressible velocity component for exothermal reactions ($\mathrm{Da} = 200$) at turbulent Mach number $M_t = 0.1$–0.8 and at $t/\tau = 34$. It is shown that the compensated spectrum of the compressible velocity component over the entire wave number range decreases slightly at $k\eta < 0.1$ with the increase of the turbulent Mach number. A narrow plateau is found at $0.02 \leqslant k\eta \leqslant 0.05$ at $M_t = 0.1$ and 0.2 where $E^{u,C}(k)\epsilon^{-2/3}k^{5/3} \approx 0.2$. This value is consistent with the observation by Wang *et al.* [47] in simulating a nonreacting compressible isotropic turbulence with a heat source at $M_t = 0.2$. The compensated spectrum of the compressible velocity component at $M_t = 0.8$ is

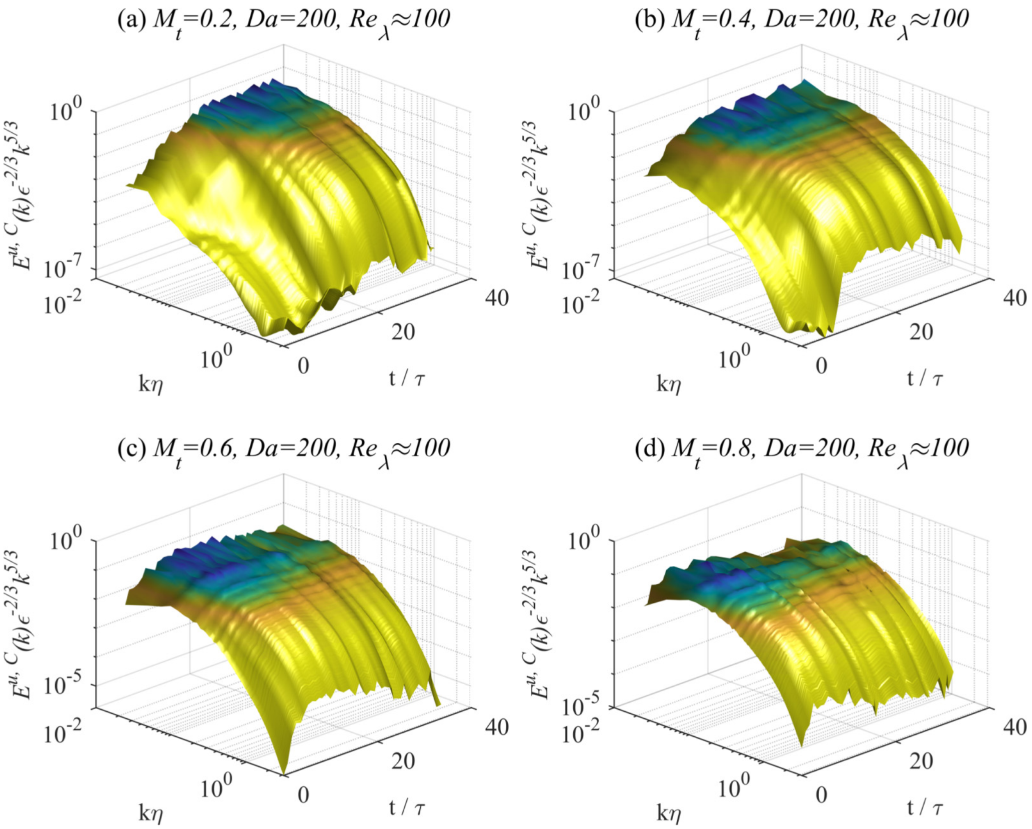

FIG. 11. Temporal variation of compensated spectrum of compressible velocity component $E^{u,C}(k)\epsilon^{-2/3}k^{5/3}$ for an exothermal reaction (Da = 200) at Taylor Reynolds number $\mathrm{Re}_\lambda \approx 100$. (a) $M_t = 0.2$, (b) $M_t = 0.4$, (c) $M_t = 0.6$, (d) $M_t = 0.8$.

larger than other cases at $k\eta > 0.4$. The effect of the turbulent Mach number on the compensated spectrum of the compressible velocity component for exothermal reactions (Da = 3000) at turbulent Mach number $M_t = 0.1$–0.6 and at $t/\tau = 34$ is shown in Fig. 12(b). A small plateau is found at $0.02 \leqslant k\eta \leqslant 0.08$ for $M_t = 0.6$ where $E^{u,C}(k)\epsilon^{-2/3}k^{5/3} \approx 0.05$. The compensated spectrum of the compressible velocity component increases with the increase of turbulent Mach number at $0.1 \leqslant k\eta \leqslant 0.4$. Figure 12(c) shows the temporal evolution of the compensated spectrum of the compressible velocity component at $M_t = 0.2$ for three reaction parameters (Da = 2, 200, 3000). It is shown that the spectrum for exothermal reactions (Da = 200, 3000) is much larger than the value for the isothermal reaction (Da = 2) over the entire wave number range. A plateau is found at $0.02 \leqslant k\eta \leqslant 0.1$ for the exothermal reaction case (Da = 3000) where $E^{u,C}(k)\epsilon^{-2/3}k^{5/3} \approx 0.2$. For the same reaction parameters (Da = 2, 200, 3000) at $M_t = 0.6$ as shown in Fig. 12(d), heat release can increase the compensated spectrum of the compressible velocity component in a finite extent. A plateau is found at $0.02 \leqslant k\eta \leqslant 0.1$ for exothermal reaction cases (Da = 200, 3000) where $E^{u,C}(k)\epsilon^{-2/3}k^{5/3} \approx 0.05$. From Figs. 12(c) and 12(d), the $k^{-5/3}$ scaling of the compressible velocity spectrum $E^{u,C}(k)$ can be found for the isothermal reaction (Da = 2) at $M_t = 0.6$. The result is consistent with the observation by Wang *et al.* [28] in simulating nonreacting compressible isotropic turbulence. For the exothermal reaction (Da = 200), the $k^{-5/3}$ scaling is found at $M_t = 0.2$ and 0.6. The result is also obtained by Wang *et al.* in simulating nonreacting compressible isotropic turbulence with heat source at $M_t = 0.2$ [47]. The scaling behavior of the compressible velocity

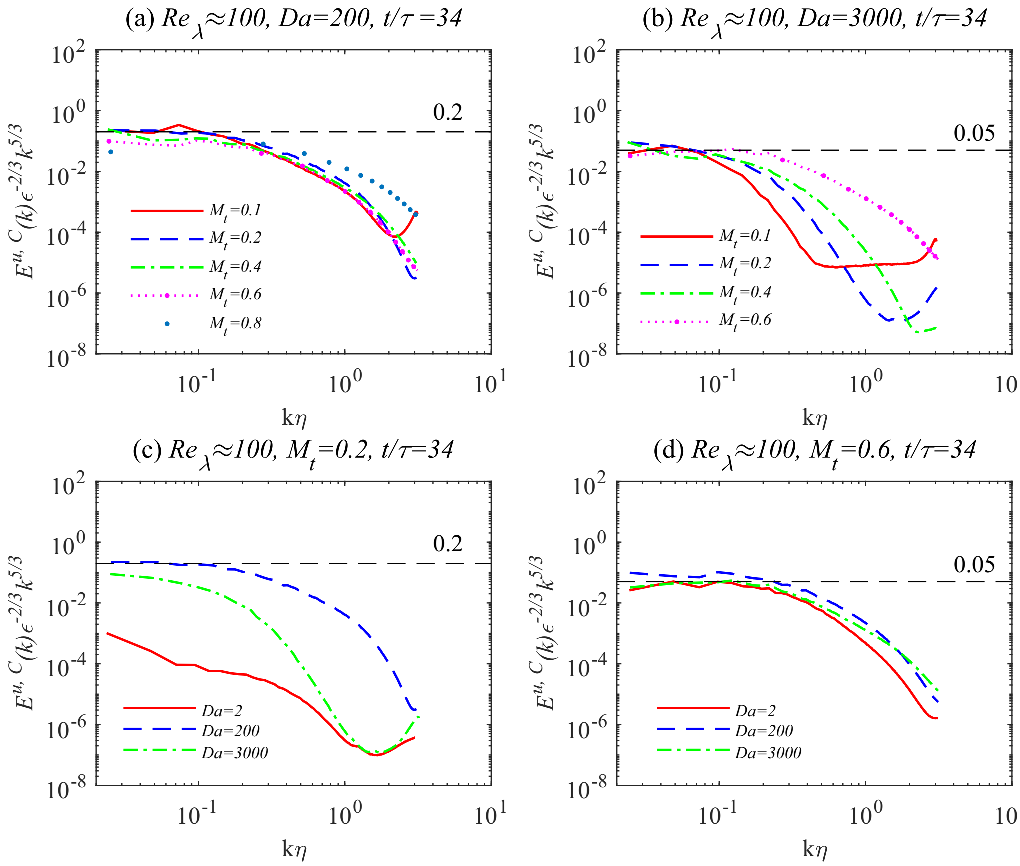

FIG. 12. Instantaneous compensated spectrum of the compressible velocity component $E^{u,C}(k)\epsilon^{-2/3}k^{5/3}$ at Taylor Reynolds number $\mathrm{Re}_\lambda \approx 100$ for three reaction parameters. (a) $M_t = 0.1$–0.8, $\mathrm{Da} = 200$, $t/\tau = 34$; (b) $M_t = 0.1$–0.6, $\mathrm{Da} = 3000$, $t/\tau = 34$; (c) $M_t = 0.2$, $\mathrm{Da} = 2$, 200, 300, $t/\tau = 34$; (d) $M_t = 0.6$, $\mathrm{Da} = 2$, 200, 300, $t/\tau = 34$.

spectrum for exothermal reactions can be attributed to the fact that the heat release can generate acoustic waves, which dominate the dynamics of the compressible velocity component at low and high turbulent Mach numbers [47].

B. Spectra of pressure, density, and temperature

In characterizing the Mach number scaling of the compressible component in turbulence, Sarkar *et al.* [27] suggested an acoustic scenario and derived an equipartition relation between the compressible velocity and compressible pressure. It is assumed that $E^{p,C}(k) \sim 2\rho_0^2 c_0^2 E^{u,C}(k)$, where c_0 is the average speed of sound, $E^{p,C}(k)$ is the spectrum of the compressible pressure component, and $E^{u,C}(k)$ is the spectrum of the compressible velocity component. The relation $E^{p,C}(k) \sim 2\rho_0^2 c_0^2 E^{u,C}(k)$ was verified at the turbulent Mach numbers $M_t = 0.3$ and 0.6 by Jagannathan and Donzis [45]. Wang *et al.* [28] further assumed that the pressure spectrum $E^p(k)$ has the same scaling as the spectrum of the compressible pressure component $E^{p,C}(k)$ at high turbulent Mach numbers and suggested the relation $E^p(k) \sim 2\rho_0^2 c_0^2 E^{u,C}(k)$ where $\int_0^\infty E^p(k)\, dk = \langle (p - p_0)^2 \rangle$. Provided the scaling of $E^{u,C}(k) \sim \epsilon^{2/3}k^{-5/3}$, the scaling for the spectrum of pressure can be expressed as $E^p(k) \sim 2\gamma \rho_0 p_0 \epsilon^{2/3} k^{-5/3}$. The spectra of density and temperature $E^\rho(k)$ and $E^T(k)$

are also investigated, where $\int_0^\infty E^\rho(k)\,dk = \langle(\rho-\rho_0)^2\rangle$ and $\int_0^\infty E^T(k)\,dk = \langle(T-T_0)^2\rangle$. For weakly compressible turbulence, Wang *et al.* [28] assumed that the fluid is nearly isentropic and the density and pressure are related as $\gamma\rho'/\rho_0 = p'/p_0$. Here $\rho' = \rho - \rho_0$ and $p' = p - p_0$, where the prime stands for the fluctuating value, and the subscript "0" stands for mean value. Similarly the fluctuations of temperature and pressure can be expressed with isentropic relation $[\gamma/(\gamma-1)]T'/T_0 = p'/p_0$ and $T' = T - T_0$. Then the spectra of density and temperature based on the isentropic relation can be expressed as $E^\rho(k) = E^p(k)\rho_0^2 p_0^{-2}\gamma^{-2}$ and $E^T(k) = E^p(k)T_0^2 p_0^{-2}[\gamma/(\gamma-1)]^{-2}$. Consequently, the following scaling relations are suggested: $E^\rho(k) \sim \epsilon^{2/3}k^{-5/3}(\gamma p_0)^{-1}(2\rho_0^3)$ and $E^T(k) \sim \epsilon^{2/3}k^{-5/3}(\gamma p_0)^{-1}[2\rho_0(\gamma-1)^2T_0^2]$.

Figure 13 shows temporal evolution of the compensated spectrum of pressure $E^p(k)\epsilon^{-2/3}k^{5/3}(2\gamma\rho_0 p_0)^{-1}$, density $E^\rho(k)\epsilon^{-2/3}k^{5/3}\gamma p_0(2\rho_0^3)^{-1}$, and temperature $E^T(k)\epsilon^{-2/3}k^{5/3}\gamma p_0[2\rho_0(\gamma-1)^2T_0^2]^{-1}$ for exothermal reactions (Da $= 200, 3000$) at Taylor Reynolds number $\mathrm{Re}_\lambda \approx 100$ and at turbulent Mach number $M_t = 0.1$ and 0.8. Figures 13(a), 13(c), and 13(e) show the compensated spectra of three thermodynamic variables at $M_t = 0.1$ for the exothermal reaction (Da $= 3000$). It is shown that the compensated spectrum of pressure increases gradually from $t/\tau = 0$–10. The compensated spectrum of pressure increases noticeably at $k\eta < 0.1$. In contrast, the compensated spectra of density and temperature increase steeply from the start of the reaction at $t/\tau = 0$ and reach the maximum value at $t/\tau \approx 3$. For the exothermal reaction (Da $= 200$) at $M_t = 0.8$ shown in Figs. 13(b), 13(d), and 13(f), the temporal evolution of the compensated spectra of three thermodynamic variables are similar to that at low turbulent Mach number cases. However, the compensated spectra elevation at the reaction initial phrase ($t/\tau = 0$–3) are not as evident as in low turbulent Mach number cases. The compensated spectra of three thermodynamic variables for exothermal reactions at low and high turbulent Mach numbers reach a nearly steady state at $t/\tau > 25$.

Figure 14(a) shows the instantaneous compensated spectrum of pressure $E^p(k)\epsilon^{-2/3}k^{5/3}(2\gamma\rho_0 p_0)^{-1}$ at $\mathrm{Re}_\lambda \approx 100$ and at turbulent Mach numbers $M_t = 0.1$–0.8 for exothermal reactions (Da $= 200$) at $t/\tau = 34$. The narrow plateau at $M_t = 0.1$ and 0.2 can be found at $0.05 < k\eta < 0.08$ where $E^p(k)\epsilon^{-2/3}k^{5/3}(2\gamma\rho_0 p_0)^{-1} \approx 0.3$. The increase of the turbulent Mach number can decrease the compensated spectrum of pressure at $k\eta < 0.1$ and increase the spectrum at $k\eta > 0.2$. Figure 14(b) shows temporal variation of the compensated spectrum of pressure at $M_t = 0.6$ for the exothermal reaction (Da $= 3000$). At the reaction initial phrase ($t/\tau = 0$–3), the compensated spectrum of pressure increases at the entire wave number range. At $t/\tau = 34$ approaching the end of the reaction, the compensated spectrum of the pressure collapses with the initial value ($t/\tau = 0$) at $k\eta > 0.05$. Figure 14(c) shows the instantaneous compensated spectrum of pressure at $\mathrm{Re}_\lambda \approx 100$ and at turbulent Mach numbers $M_t = 0.1$ for three reaction parameters at $t/\tau = 34$. It is shown that exothermal reactions (Da $= 200, 3000$) can increase the compensated spectrum of pressure. For the exothermal reaction (Da $= 200$), the spectrum elevation is primarily found at $k\eta < 0.2$, while for the exothermal reaction (Da $= 3000$), the spectrum is overall elevated at the entire wave number range. For the same Taylor Reynolds number and reaction time at $M_t = 0.6$ shown in Fig. 14(d), the compensated spectrum of pressure increases for exothermal reactions (Da $= 200, 3000$) at $k\eta > 0.3$.

Figure 15 shows the instantaneous spectrum of pressure-dilatation $E^{p\theta}(k)$ at $\mathrm{Re}_\lambda \approx 100$ and at turbulent Mach numbers $M_t = 0.1$ and 0.8 for isothermal (Da $= 2$) and exothermal (Da $= 200$) reactions, where $\int_0^\infty E^{p\theta}(k)\,dk = \langle[(p-p_0)\partial u_i/\partial x_i]^2\rangle$. For isothermal reactions (Da $= 2$) at M_t=0.1 and 0.8 as shown in Figs. 15(a) and 15(c), respectively, the spectra nearly collapse with each other during the entire reaction process. The observation suggests that the spectra of pressure dilatation are nearly unaffected by isothermal reactions in a wide range of length scales. For exothermal reactions (Da $= 200$) at $M_t = 0.1$ and 0.8 as shown in Figs. 15(b) and 15(d), respectively, the spectrum increases at the entire $k\eta$ scales at $t/\tau > 0$. For the exothermal (Da $= 200$) reaction at $M_t = 0.1$ as shown in Fig. 15(b), the spectrum of the pressure dilatation at $t/\tau = 34$ is larger than the initial spectrum ($t/\tau = 0$). For the exothermal reaction (Da $= 200$) at

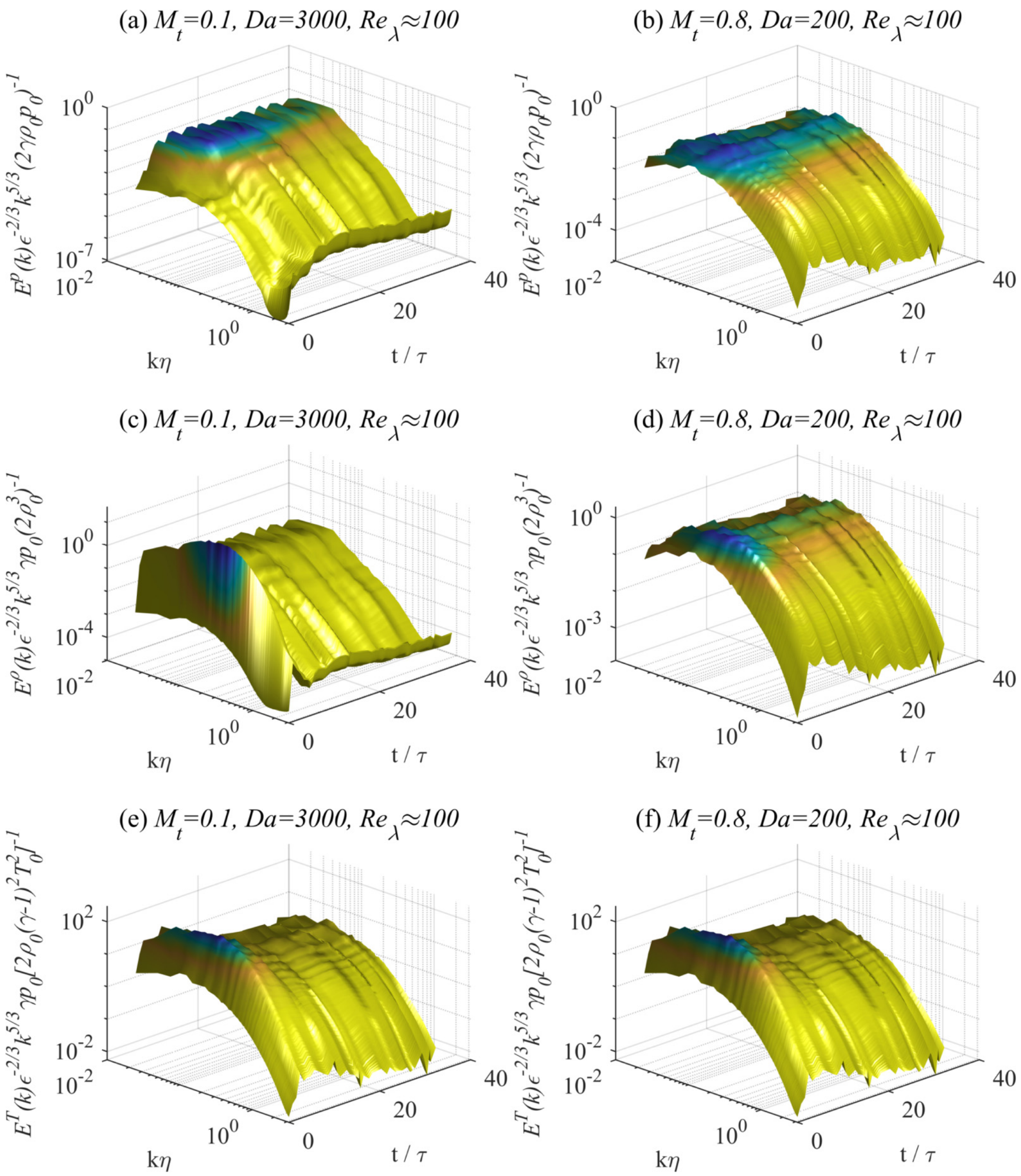

FIG. 13. Temporal variation of compensated spectra of pressure, density, and temperature for exothermal reactions (Da = 200, 3000) at Taylor Reynolds number $\mathrm{Re}_\lambda \approx 100$ at different turbulent Mach numbers: (a, b) $E^p(k)\epsilon^{-2/3}k^{5/3}(2\gamma\rho_0 p_0)^{-1}$, (c, d) $E^\rho(k)\epsilon^{-2/3}k^{5/3}\gamma p_0(2\rho_0^3)^{-1}$, (e, f) $E^T(k)\epsilon^{-2/3}k^{5/3}\gamma p_0[2\rho_0(\gamma-1)^2T_0^2]^{-1}$.

$M_t = 0.8$ as shown in Fig. 15(d), the spectra at t/τ=0 and 34 nearly collapse with each other at $k\eta < 1$.

To derive the Mach number scaling of thermodynamic variables, the acoustic scenario [27] and isentropic relations [28] are used. To verify those assumptions in reacting compressible isentropic turbulence, Fig. 16 shows the comparison of the compensated spectra of pressure $E^p(k)\epsilon^{-2/3}k^{5/3}(2\gamma\rho_0 p_0)^{-1}$, density $E^\rho(k)\epsilon^{-2/3}k^{5/3}\gamma p_0(2\rho_0^3)^{-1}$, and temperature $E^T(k)\epsilon^{-2/3}k^{5/3}\gamma p_0[2\rho_0(\gamma-1)^2T_0^2]^{-1}$ at $M_t = 0.1$–0.8 for exothermal reactions (Da = 200, 3000). It can be found that at $M_t = 0.1$ for the exothermal reaction (Da = 200), the

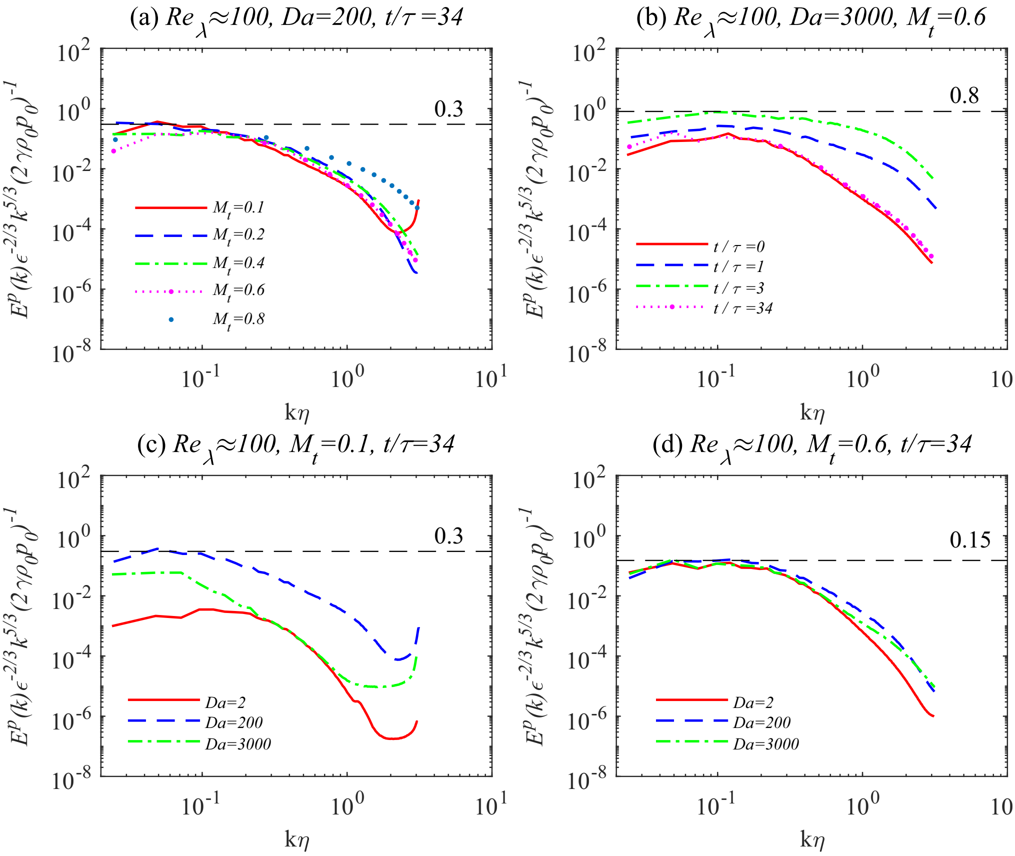

FIG. 14. Instantaneous compensated spectrum of pressure $E^p(k)\epsilon^{-2/3}k^{5/3}(2\gamma\rho_0p_0)^{-1}$ at Taylor Reynolds number $\mathrm{Re}_\lambda \approx 100$ for three reaction parameters: (a) $M_t = 0.1$–0.8, $\mathrm{Da} = 200$, $t/\tau = 34$; (b) $M_t = 0.6$, $\mathrm{Da} = 3000$, $t/\tau = 0$–34; (c) $M_t = 0.1$, $\mathrm{Da} = 2, 200, 3000$, $t/\tau = 34$; (d) $M_t = 0.6$, $\mathrm{Da} = 2, 200, 3000$, $t/\tau = 34$.

compensated spectra of three thermodynamic variables collapse with each other at $k\eta < 1.5$ as shown in Fig. 16(a). For the exothermal reaction ($\mathrm{Da} = 3000$) at $M_t = 0.2$, collapse of the three compensated spectra is observed at $k\eta < 0.3$ as shown in Fig. 16(c). At $M_t = 0.8$ for the exothermal reaction ($\mathrm{Da} = 200$) and at $M_t = 0.6$ for the exothermal reaction ($\mathrm{Da} = 3000$) shown in Figs. 16(b) and 16(d), respectively, the compensated spectra of the three thermodynamic variables nearly collapse with each other at the entire wave number range. The compensated spectra of three thermodynamic variables collapse with each other at low and high turbulent Mach numbers for exothermal reactions, indicating that the isentropic assumption is valid in current simulations.

To verify the isentropic relations among the fluctuations of pressure, density, and temperature, Wang *et al.* [28] defined the residual density and residual temperature as $\rho^R = \rho' - \rho_0 p'/(\gamma p_0)$ and $T^R = T' - (\gamma - 1)T_0 p'/(\gamma p_0)$. Figure 17 shows the normalized spectra of the residual density and residual temperature, $E_R^\rho(k)/E^\rho(k)$ and $E_R^T(k)/E^T(k)$ at turbulent Mach numbers $M_t = 0.1$–0.8 for exothermal reactions ($\mathrm{Da} = 200, 3000$) and Taylor Reynolds number $\mathrm{Re}_\lambda \approx 100$ at $t/\tau = 34$. Here $\int_0^\infty E_R^\rho(k)\,dk = \langle(\rho^R)^2\rangle$ and $\int_0^\infty E_R^T(k)\,dk = \langle(T^R)^2\rangle$. It is shown that the normalized spectra of the residual density and residual temperature are much smaller than 1.0 in the range of $k\eta \leqslant 0.1$, indicating that the spectra of density and temperature exhibit the same inertial scaling as the spectrum of pressure in chemically reacting compressible turbulence. The normalized spectra of

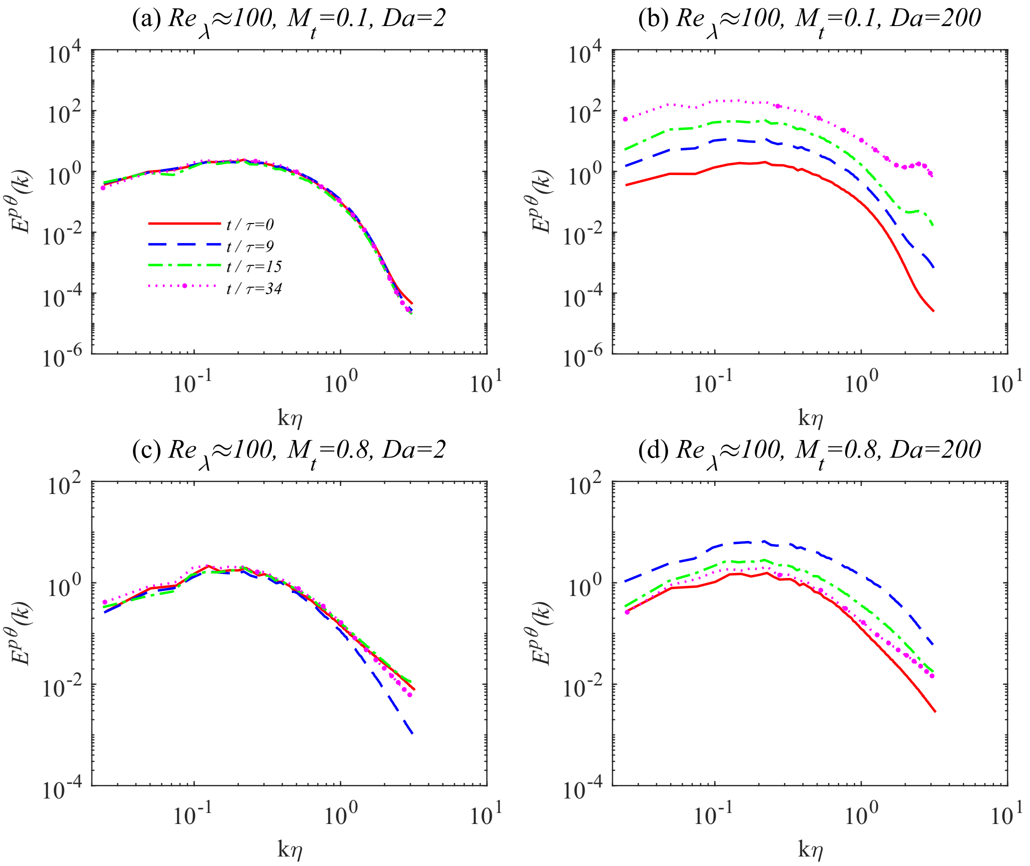

FIG. 15. Instantaneous spectrum of pressure dilatation $E^{p\theta}(k)$ at Taylor Reynolds number $\mathrm{Re}_\lambda \approx 100$. (a) $M_t = 0.1$, $\mathrm{Da} = 2$; (b) $M_t = 0.1$, $\mathrm{Da} = 200$; (c) $M_t = 0.8$, $\mathrm{Da} = 2$; (d) $M_t = 0.8$, $\mathrm{Da} = 200$.

the residual density and residual temperature approach 1.0 at $k\eta \approx 1$, indicating that the isentropic relations are no longer valid at small scales $k\eta \approx 1$.

The strong acoustic equilibrium indicates that the spectra of compressible velocity and pressure can overlap each other by a proper normalization [27,41,45]. Figure 18 shows the normalized pressure fluctuation spectrum $E^p(k)/(p_{\mathrm{rms}})^2$ and the normalized spectrum of the compressible velocity component $2E^{u,C}(k)/(u^C_{\mathrm{rms}})^2$ at $M_t = 0.1$–0.6 and at Taylor Reynolds number $\mathrm{Re}_\lambda \approx 100$ approaching the end of reaction ($t/\tau = 34$) for exothermal reactions ($\mathrm{Da} = 200$, $\mathrm{Da} = 3000$). It can be found that the normalized spectra of pressure and compressible velocity component collapse with each other for exothermal reactions at $M_t = 0.1$–0.6. At $M_t = 0.2$–0.6 for two exothermal reactions ($\mathrm{Da} = 200, 3000$) shown in Figs. 18(b)–18(d), the $k^{-5/3}$ power-law scaling is found at $k\eta < 0.1$. The spectra shown in Fig. 18 indicate that at both low and high turbulent Mach numbers, the dynamics of the compressible velocity and the pressure is dominated by acoustic waves generated by heat release for exothermal reactions in compressible turbulence.

V. ONE-POINT STATISTICS AND MACH NUMBER SCALING

Analysis of spectra in the previous section suggests that the variation of one-point statistics can be related with turbulent Mach number and heat release through chemical reactions. Several one-point statistics are analyzed in this section, including the ratio of compressible to solenoidal kinetic energy

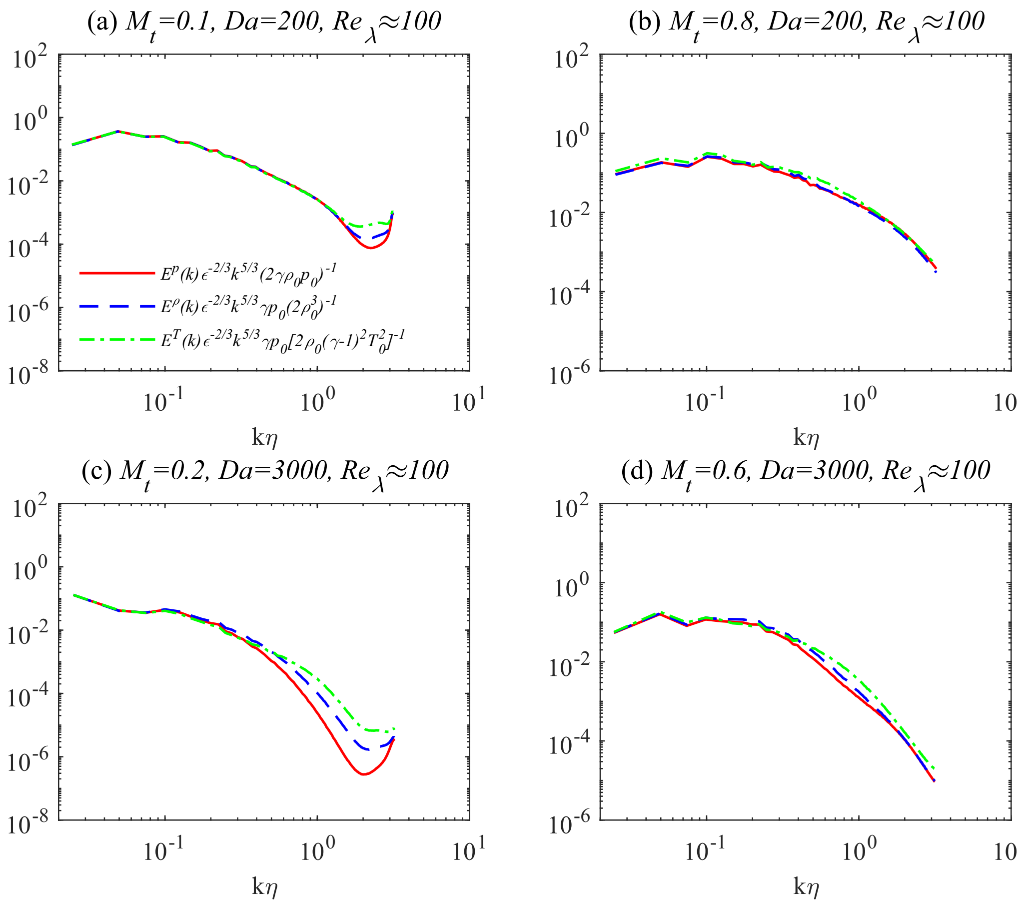

FIG. 16. Compensated spectra of pressure $E^p(k)\epsilon^{-2/3}k^{5/3}(2\gamma\rho_0p_0)^{-1}$, density $E^\rho(k)\epsilon^{-2/3}k^{5/3}\gamma p_0(2\rho_0^3)^{-1}$, and temperature $E^T(k)\epsilon^{-2/3}k^{5/3}\gamma p_0[2\rho_0(\gamma-1)^2T_0^2]^{-1}$ at $M_t = 0.1$–0.8 for exothermal reactions (Da = 200, 3000) at Taylor Reynolds number $\mathrm{Re}_\lambda \approx 100$. (a) $M_t = 0.1$, Da = 200; (b) $M_t = 0.8$, Da = 200; (c) $M_t = 0.2$, Da = 3000; (d) $M_t = 0.6$, Da = 3000.

and ratio of the compressible component to solenoidal component of kinetic energy dissipation as well as rms values of the velocity and thermodynamic variables based on statistical steady flow data from $t/\tau = 25$–34. Figure 19 shows the ratio of compressible to solenoidal kinetic energy K^c/K^s and the ratio of the compressible component to solenoidal component of kinetic energy dissipation ϵ^c/ϵ^s for three reaction parameters at turbulent Mach number $M_t = 0.1$–1.0 and at different Taylor Reynolds numbers. Here $K^c = \langle[(u_1^c)^2 + (u_2^c)^2 + (u_3^c)^2]/2\rangle$ and $K^s = \langle[(u_1^s)^2 + (u_2^s)^2 + (u_3^s)^2]/2\rangle$, respectively. $\epsilon^c = \langle 4\mu/(3\,\mathrm{Re}\,\rho)\rangle\langle\theta^2\rangle$ and $\epsilon^s = \langle\mu/(\mathrm{Re}\,\rho)\rangle\langle\omega_i\omega_i\rangle$, respectively [23,28,44,45]. At a fixed turbulent Mach number, a larger Taylor Reynolds number results in a slightly higher normalized compressible kinetic energy K^c/K^s for three reaction parameters as shown in Fig. 19(a). For isothermal reaction cases (Da = 2), there is no single Mach scaling suitable to encompass variation of the normalized compressible kinetic energy K^c/K^s from $M_t = 0.1$ to 1.0. For the $M_t < 0.4$ cases, $K^c/K^s \sim M_t^4$. The result is consistent with the improved EDQNM model proposed by Fauchet and Bertoglio [48] for small turbulent Mach number turbulence and the pseudosound relation proposed by Ristorcelli [26]. For the $M_t \geqslant 0.4$ cases, $K^c/K^s \sim M_t^2$. Those findings are consistent with the scaling laws found in nonreacting compressible homogeneous isotropic turbulence [40]. For exothermal reaction cases (Da = 200, 3000), the normalized compressible kinetic energy K^c/K^s

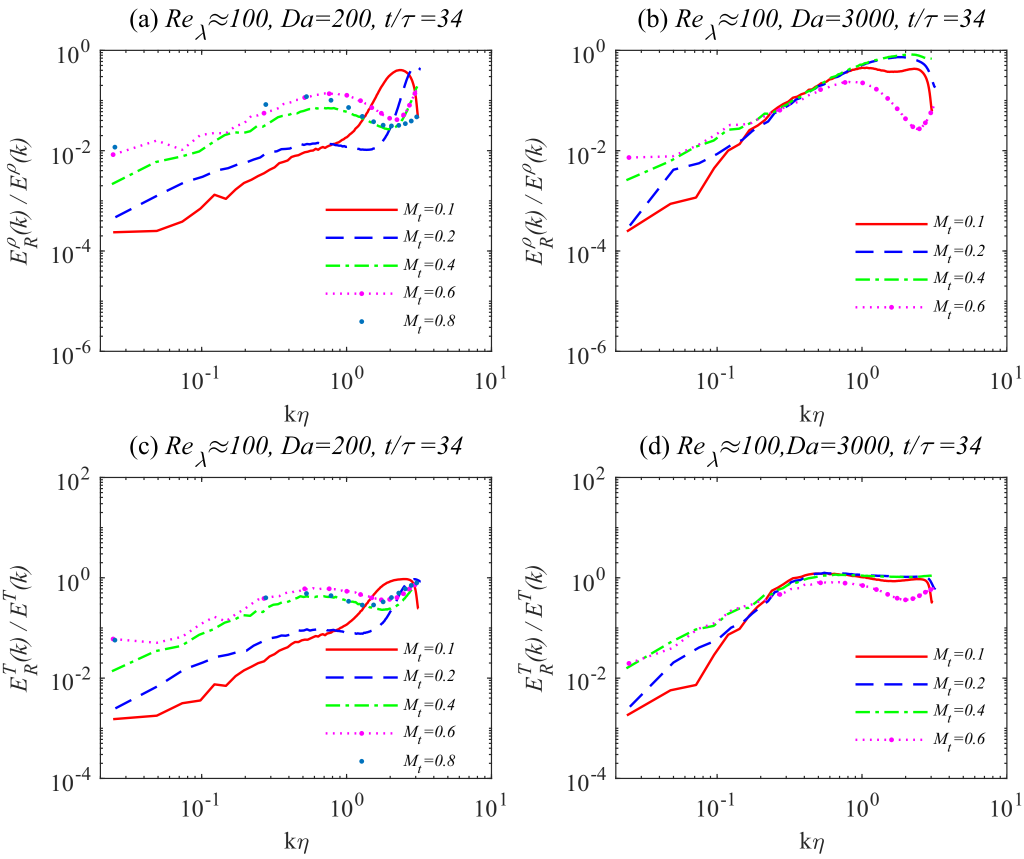

FIG. 17. Normalized spectra of the residual density (a, b) and residual temperature (c, d) at turbulent Mach numbers $M_t = 0.1$–0.8 and at Taylor Reynolds number $\mathrm{Re}_\lambda \approx 100$ for exothermal reactions (Da = 200, 3000) at $t/\tau = 34$.

is nearly independent of the turbulent Mach number. It is found that $K^c/K^s \approx 0.1$ and 0.025 for the reaction case Da = 200 and reaction case Da = 3000, respectively. A larger heat release rate results in a higher K^c/K^s value in exothermal reactions. For the ratio of compressible component to solenoidal component of kinetic energy dissipation ϵ^c/ϵ^s, a higher Taylor Reynolds number results in larger ϵ^c/ϵ^s at a fixed turbulent Mach number as shown in Fig. 19(b). In isothermal reaction cases at $M_t < 0.4$, $\epsilon^c/\epsilon^s \sim M_t^4$, and for $M_t \geqslant 0.4$, $\epsilon^c/\epsilon^s \sim M_t^5$. In low turbulent Mach number nonreacting turbulence, the pseudosound constitutive analysis proposed by Ristorcelli [26] and the improved EDQNM model proposed by Fauchet and Bertoglio [48] suggested the M_t^4 scaling for ϵ^c/ϵ^s. For higher turbulent Mach number situations, a M_t^5 scaling for ϵ^c/ϵ^s is predicted by the EDQNM model [26]. The above Mach number scalings are applicable in isothermal reacting turbulence. For exothermal reaction cases, the ratio of the compressible component to solenoidal component of kinetic energy dissipation is also nearly independent of turbulent Mach number. $\epsilon^c/\epsilon^s \approx 0.1$ and 0.01 for the reaction case Da = 200 and reaction case Da = 3000, respectively.

The normalized rms values of pressure, density, and temperature are also investigated. Figure 20 shows the Mach scaling of normalized rms values of pressure p_{rms}/p_0, density $\gamma\rho_{\mathrm{rms}}/\rho_0$, and temperature $\gamma T_{\mathrm{rms}}/[(\gamma-1)T_0]$ for three reaction parameters at turbulent Mach number $M_t = 0.1$–1.0 and at different Taylor Reynolds numbers. Here the rms values of pressure, density, and

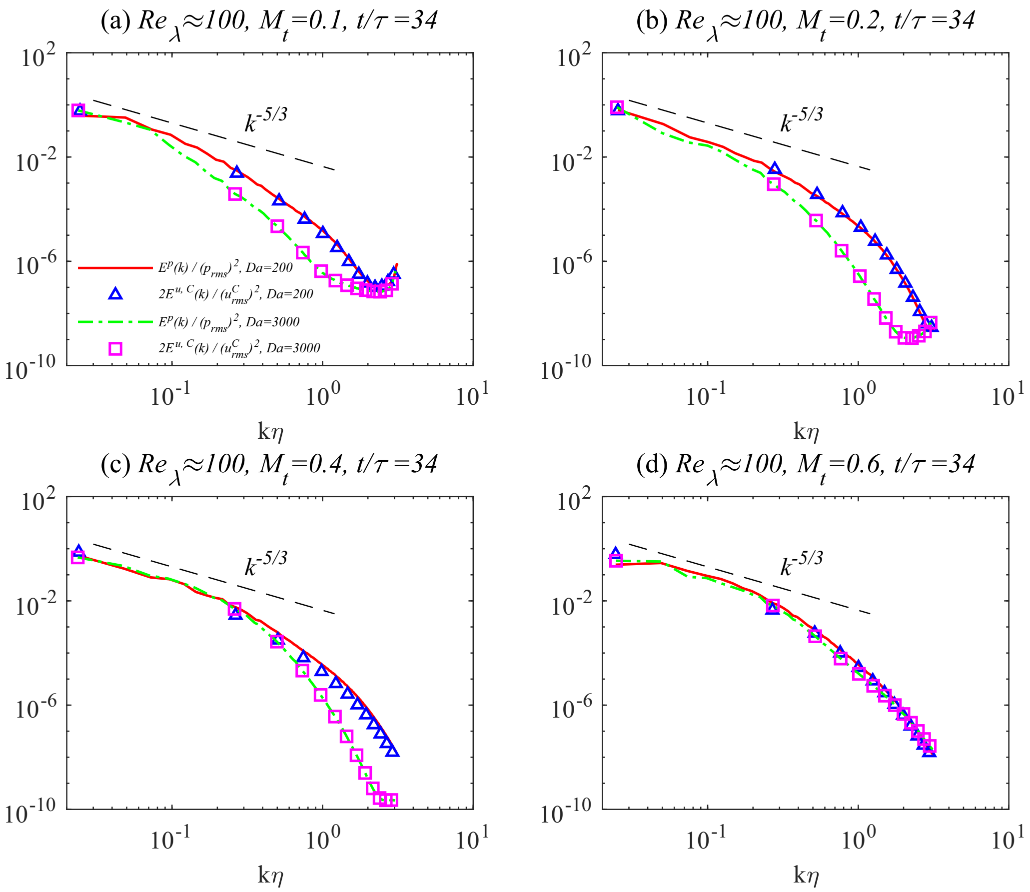

FIG. 18. Normalized spectra of pressure and compressible velocity component at Taylor Reynolds number $\mathrm{Re}_\lambda \approx 100$ for exothermal reactions (Da = 200, 3000): (a) $M_t = 0.1$, (b) $M_t = 0.2$, (c) $M_t = 0.4$, (d) $M_t = 0.6$.

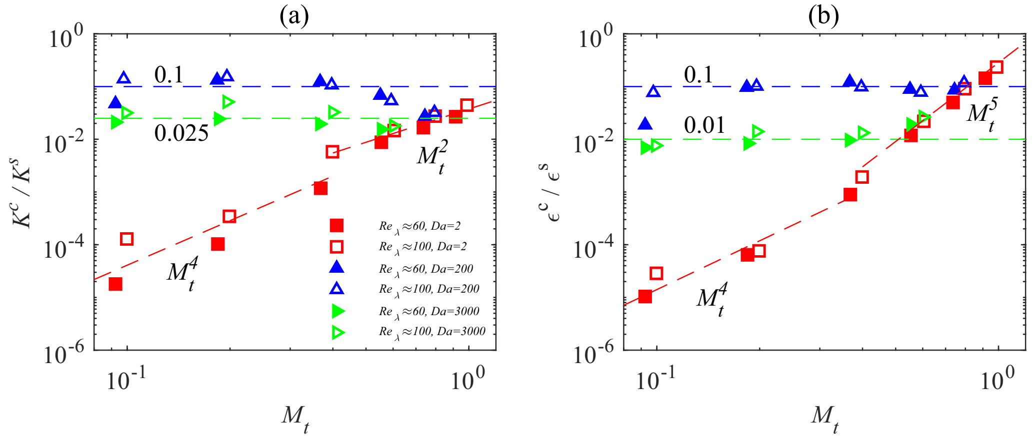

FIG. 19. (a) Ratio of compressible to solenoidal kinetic energy K^c/K^s; (b) ratio of compressible component to solenoidal component of kinetic energy dissipation ϵ^c/ϵ^s as a function of M_t.

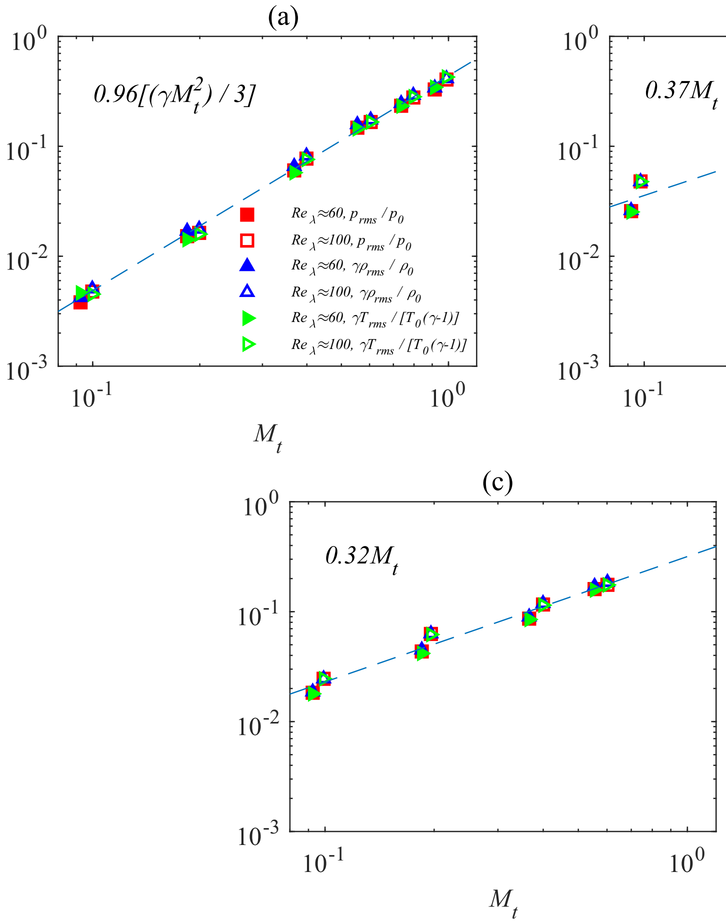

FIG. 20. Normalized rms values of pressure, density, and temperature at different turbulent Mach numbers and Taylor Reynolds numbers: (a) Da = 2; (b) Da = 200; (c) Da = 3000.

temperature are $p_{\mathrm{rms}} = \sqrt{\langle (p - p_0)^2 \rangle}$, $\rho_{\mathrm{rms}} = \sqrt{\langle (\rho - \rho_0)^2 \rangle}$ and $T_{\mathrm{rms}} = \sqrt{\langle (T - T_0)^2 \rangle}$, respectively [28]. For incompressible nonreacting turbulence, the rms value of pressure has the following relation: $p_{\mathrm{rms}} = \sqrt{\langle (p - p_0)^2 \rangle} \approx A\rho_0 u'^2/3$, where $u' = \sqrt{\langle u_1^2 + u_2^2 + u_3^2 \rangle}$ and $A = 0.92$ [28,49]. The normalized rms value of pressure in compressible turbulence can be derived with the relation $u'^2 \approx M_t^2 \gamma p_0/\rho_0$ [28],

$$p_{\mathrm{rms}}/p_0 \approx \frac{A\gamma}{3} M_t^2. \tag{18}$$

In normalization, γ and $\gamma(\gamma - 1)$ are determined based on isentropic relations: $\gamma \rho'/\rho_0 = p'/p_0$ and $[\gamma/(\gamma - 1)]T'/T_0 = p'/p_0$. Therefore, the following relations for normalized rms values of density and temperature are defined [28]:

$$\rho_{\mathrm{rms}}/\rho_0 \approx \frac{A}{3} M_t^2, \tag{19}$$

$$T_{\mathrm{rms}}/T_0 \approx \frac{A(\gamma - 1)}{3} M_t^2. \tag{20}$$

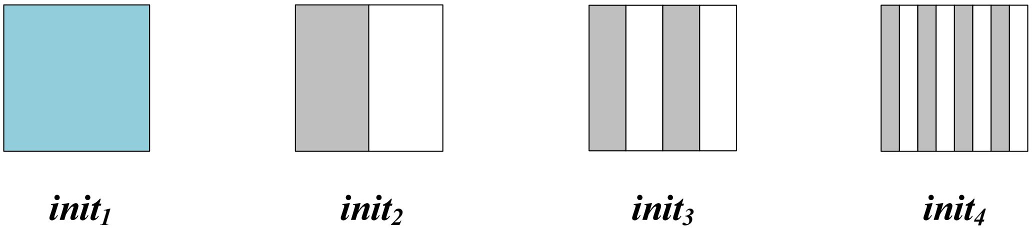

FIG. 21. Initial density field at the start of chemical reactions. $init_1$: homogeneous distribution of Y_A and Y_B, $Y_A = 0.5$, $Y_B = 0.5$; $init_2 \sim init_4$: gray slab $Y_A = 0.99$, $Y_B = 0.01$, white slab $Y_A = 0.01$, $Y_B = 0.99$.

For isothermal reactions (Da = 2) shown in Fig. 20(a), the $A[(\gamma M_t{}^2)/3]$ relation is found for the normalized rms value of pressure where $A = 0.96$. The coefficient A slightly deviates from the value (0.92) reported in the literature [28,49]. In contrast, for the exothermal reaction cases (Da = 200, 3000) shown in Figs. 20(b) and 20(c), respectively, the relations for normalized rms values of pressure, density, and temperature are no longer applicable. It is found that the normalized

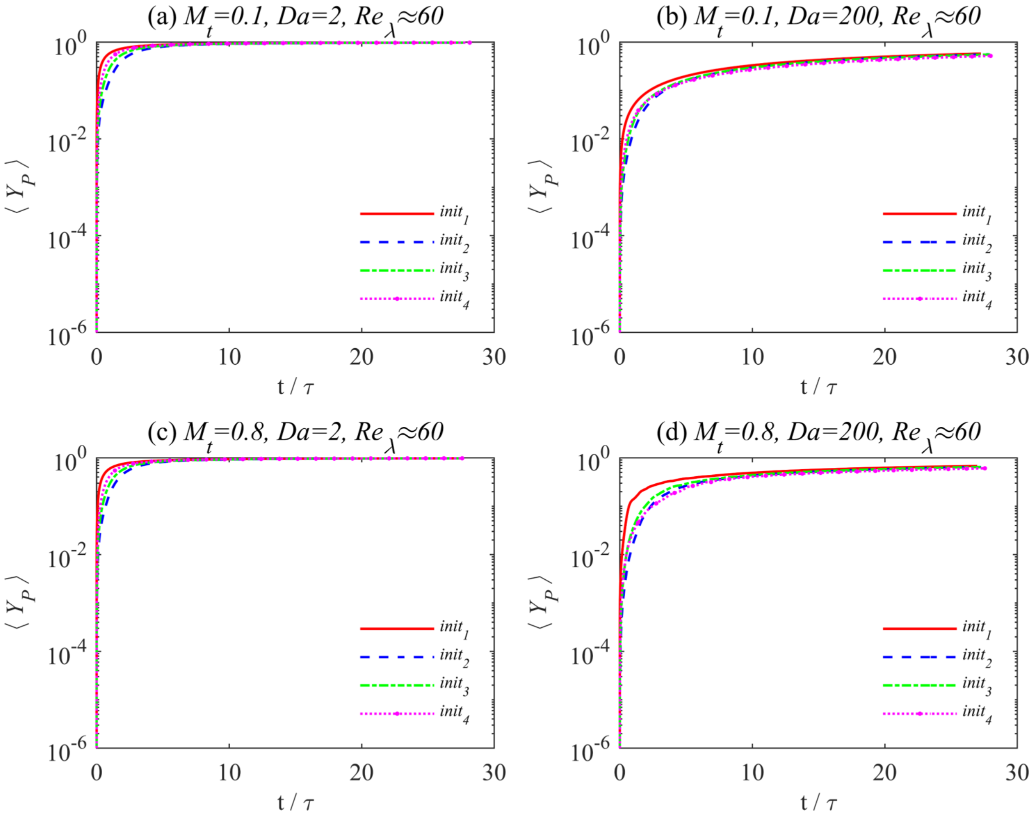

FIG. 22. Temporal variation of mass fraction of product P at $M_t = 0.1$ and 0.8 at $\mathrm{Re}_\lambda \approx 60$ for isothermal (Da = 2) and exothermal (Da = 200) reactions. (a) $M_t = 0.1$, Da = 2; (b) $M_t = 0.1$, Da = 200; (c) $M_t = 0.8$, Da = 2; (d) $M_t = 0.8$, Da = 200.

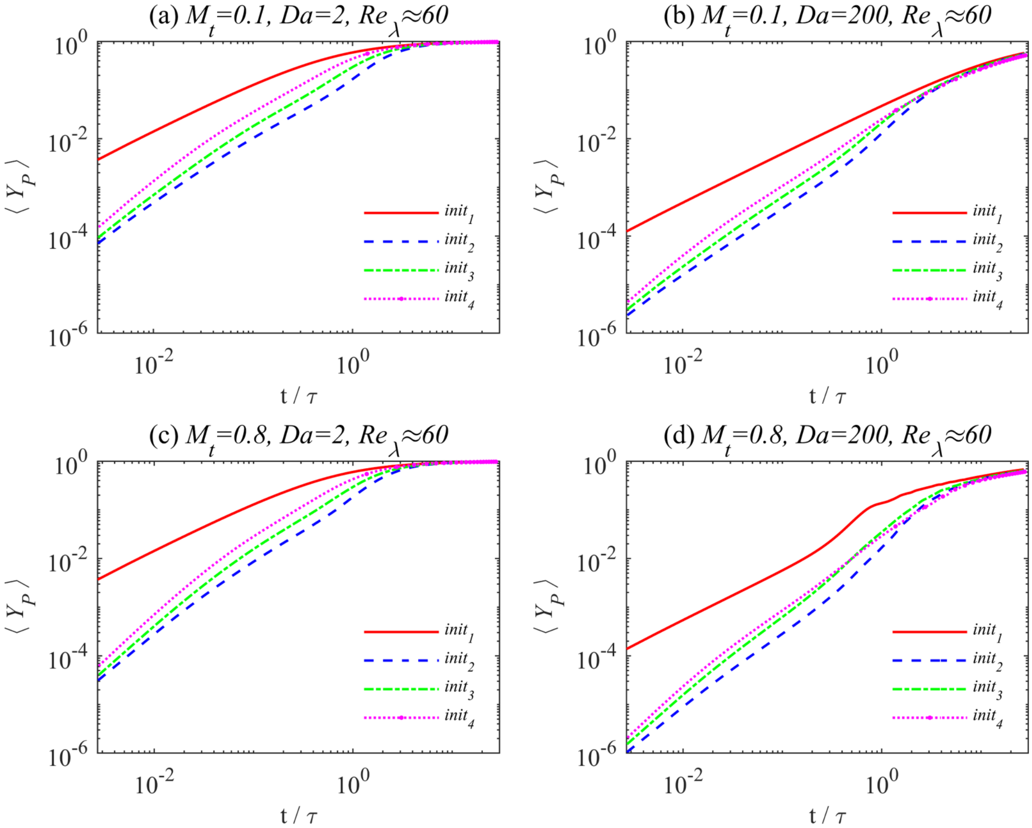

FIG. 23. Temporal variation of mass fraction of product P at $M_t = 0.1$ and 0.8 at $\mathrm{Re}_\lambda \approx 60$ for isothermal ($\mathrm{Da} = 2$) and exothermal ($\mathrm{Da} = 200$) reactions, log-log scale. (a) $M_t = 0.1$, $\mathrm{Da} = 2$; (b) $M_t = 0.1$, $\mathrm{Da} = 200$; (c) $M_t = 0.8$, $\mathrm{Da} = 2$; (d) $M_t = 0.8$, $\mathrm{Da} = 200$.

rms values exhibit a M_t scaling:

$$p_{\mathrm{rms}}/p_0 \approx BM_t, \tag{21}$$

$$\rho_{\mathrm{rms}}/\rho_0 \approx \frac{B}{\gamma}M_t, \tag{22}$$

$$T_{\mathrm{rms}}/T_0 \approx \frac{B(\gamma-1)}{\gamma}M_t, \tag{23}$$

where $B = 0.37$ and 0.32 for case $\mathrm{Da} = 200$ and $\mathrm{Da} = 3000$, respectively.

VI. CONCLUDING REMARKS

In this paper, the spectra and statistics of velocity and thermodynamic variables in chemically reacting compressible isotropic turbulence driven by a large-scale solenoidal force at turbulent Mach number $M_t = 0.1$–1.0 and at the Taylor Reynolds number from 54 to 103 were numerically studied. A single-step irreversible Arrhenius-type chemical reaction is implemented to evaluate the chemical reaction influence on spectra and statistics. Three sets of reaction parameters are used to determine the reaction rate and heat release rate.

In isothermal reactions, the spectra of velocity and thermodynamic variables as well as one-point statistics are unaffected by chemical reactions. For weakly compressible turbulence at turbulent

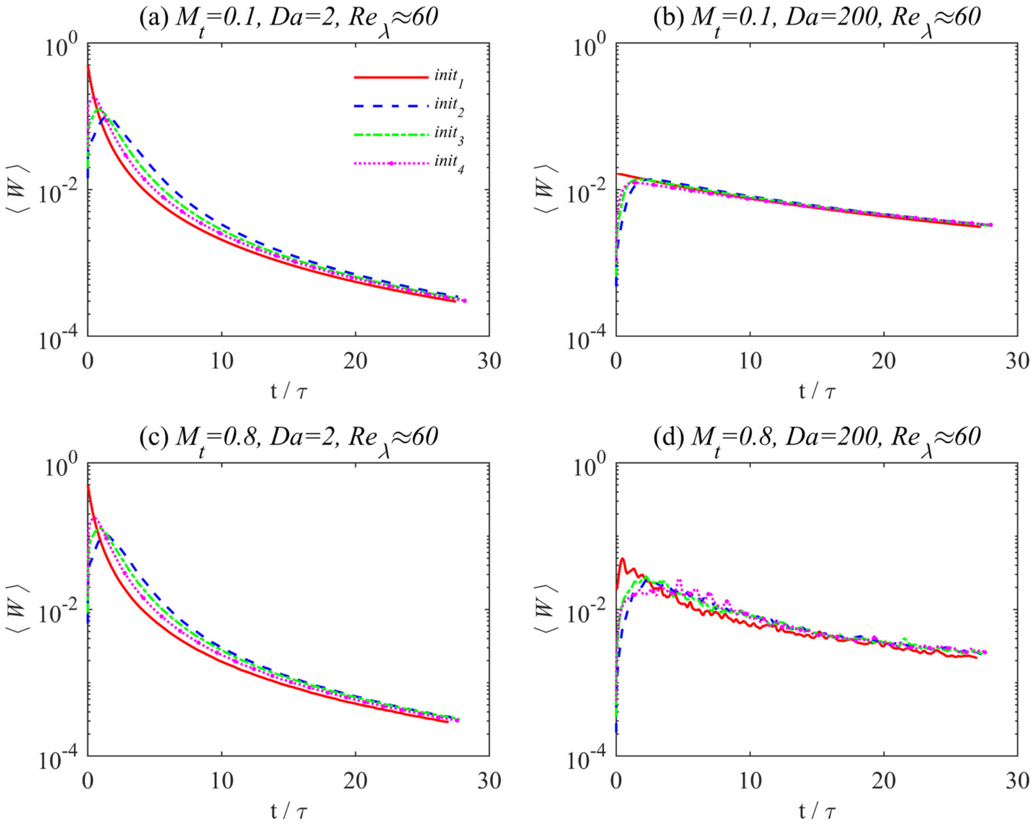

FIG. 24. Temporal variation of reaction rate W at $M_t = 0.1$ and 0.8 at $\mathrm{Re}_\lambda \approx 60$ for isothermal (Da = 2) and exothermal (Da = 200) reactions. (a) $M_t = 0.1$, Da = 2; (b) $M_t = 0.1$, Da = 200; (c) $M_t = 0.8$, Da = 2; (d) $M_t = 0.8$, Da = 200.

Mach number $M_t < 0.4$, both the ratio of compressible kinetic energy to solenoidal kinetic energy K^c/K^s and the ratio of compressible dissipation to solenoidal dissipation ϵ^c/ϵ^s exhibit a M_t^4 scaling. For moderate and strong compressible turbulence at $M_t \geqslant 0.4$, M_t^2 and M_t^5 scalings are found for K^c/K^s and ϵ^c/ϵ^s, respectively. The normalized rms values of pressure, density, and temperature exhibit a M_t^2 scaling. The above observations are consistent with the results previously obtained in nonreacting compressible turbulence. The isothermal reactions will not significantly change the spectra and one-point statistics of the flow variables in compressible isotropic turbulence.

Heat release through exothermal reactions can apparently promote species mixing and thus results in a larger reaction rate beyond the initial reaction phrase. Heat release can enhance the spectra of temperature, density, compressible velocity component, and pressure. For the same reaction parameters, the increase of spectra due to heat release is more prominent at lower turbulent Mach number cases, as compared to the cases of a higher turbulent Mach number. The ratio of the compressible kinetic energy to solenoidal kinetic energy K^c/K^s and the ratio of compressible dissipation to solenoidal dissipation ϵ^c/ϵ^s in exothermal reactions are nearly independent of turbulent Mach number. The normalized rms values of pressure, density, and temperature exhibit a M_t scaling. The spectra of the pressure and compressible velocity satisfy the strong acoustic equilibrium relation at turbulent Mach number $M_t = 0.1$–0.6, indicating that the acoustic mode dominates over the dynamics of compressible velocity and pressure.

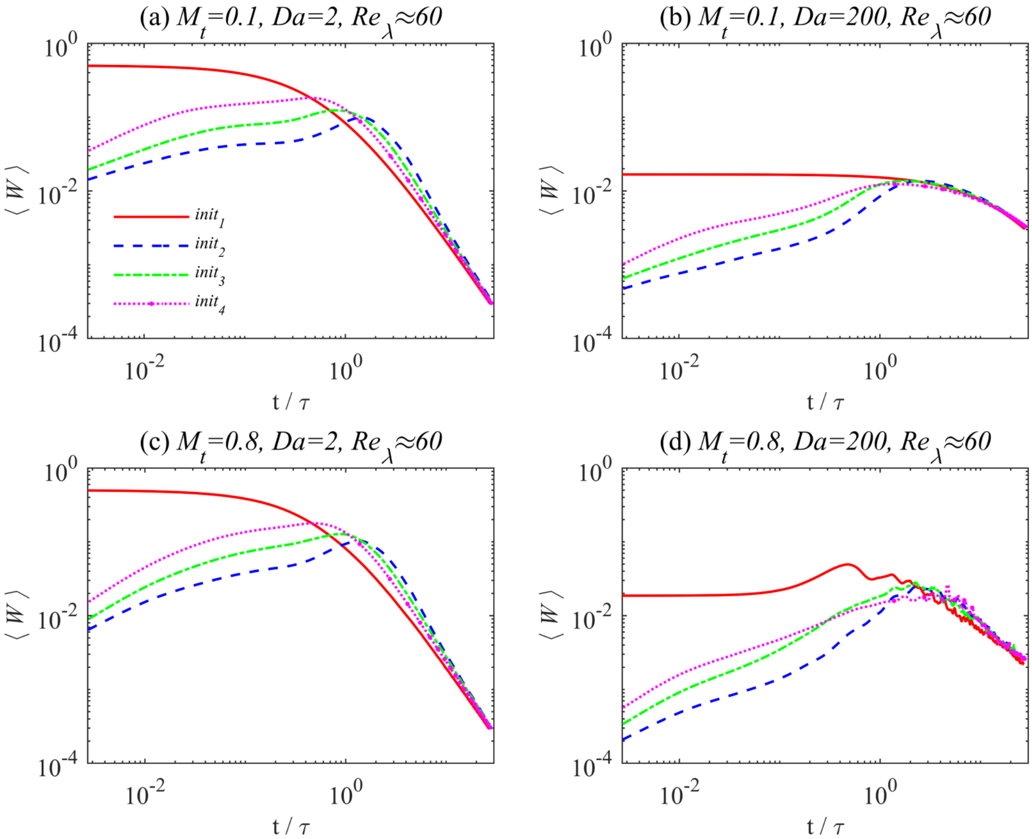

FIG. 25. Temporal variation of reaction rate W at $M_t = 0.1$ and 0.8 at $\mathrm{Re}_\lambda \approx 60$ for isothermal ($\mathrm{Da} = 2$) and exothermal ($\mathrm{Da} = 200$) reactions, log-log scale. (a) $M_t = 0.1$, $\mathrm{Da} = 2$; (b) $M_t = 0.1$, $\mathrm{Da} = 200$; (c) $M_t = 0.8$, $\mathrm{Da} = 2$; (d) $M_t = 0.8$, $\mathrm{Da} = 200$.

ACKNOWLEDGMENTS

This work was supported by National Numerical Windtunnel Project, the National Natural Science Foundation of China (NSFC Grants No. 91952104, No. 11702127, and No. 91752201), the Technology and Innovation Commission of Shenzhen Municipality (Grants No. KQTD20180411143441009, No. JCYJ20170412151759222, and No. ZDSYS201802081843517), the Key Special Project for Introduced Talents Team of Southern Marine Science and Engineering Guangdong Laboratory (Guangzhou) (Grant No. GML2019ZD0103), and the Department of Science and Technology of Guangdong Province (Grant No. 2019B21203001). This work was also supported by the Center for Computational Science and Engineering of Southern University of Science and Technology. J.W. acknowledges support from the Young Elite Scientist Sponsorship Program by CAST (Grant No. 2016QNRC001).

APPENDIX A: DERIVATION OF DIMENSIONLESS N-S EQUATIONS

The dimensional N-S equations are given as follows [50,51] where the superscript "d" denotes dimensional variables:

$$\frac{\partial \rho^d}{\partial t^d} + \frac{\partial \left(\rho^d u_j^d\right)}{\partial x_j^d} = 0, \tag{A1}$$

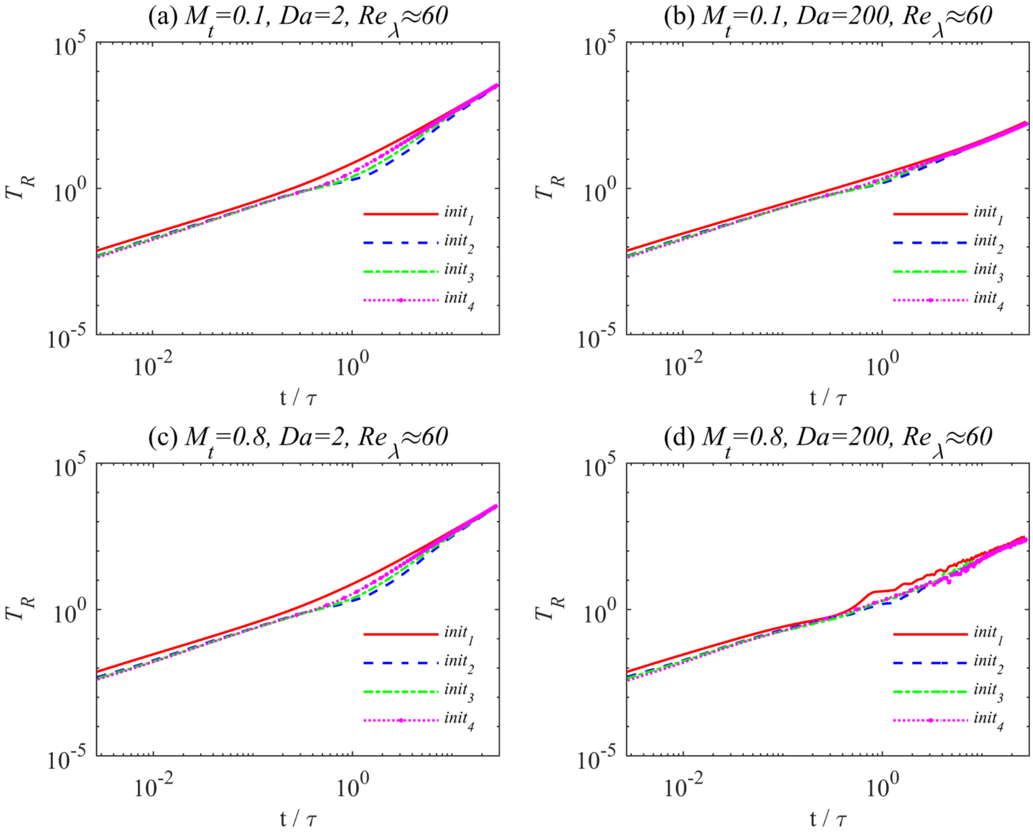

FIG. 26. Temporal variation of reaction timescale T_R at $M_t = 0.1$ and 0.8 at $\mathrm{Re}_\lambda \approx 60$ for isothermal ($\mathrm{Da} = 2$) and exothermal ($\mathrm{Da} = 200$) reactions, log-log scale. (a) $M_t = 0.1$, $\mathrm{Da} = 2$; (b) $M_t = 0.1$, $\mathrm{Da} = 200$; (c) $M_t = 0.8$, $\mathrm{Da} = 2$; (d) $M_t = 0.8$, $\mathrm{Da} = 200$.

$$\frac{\partial\left(\rho^d u_i^d\right)}{\partial t^d} + \frac{\partial\left[\rho^d u_i^d u_j^d + p^d \delta_{ij}\right]}{\partial x_j^d} = \frac{\partial \sigma_{ij}^d}{\partial x_j^d}, \tag{A2}$$

$$\frac{\partial \mathcal{E}^d}{\partial t^d} + \frac{\partial\left[(\mathcal{E}^d + p^d) u_j^d\right]}{\partial x_j^d} = \frac{\partial}{\partial x_j^d}\left(\kappa^d \frac{\partial T^d}{\partial x_j^d}\right) + \frac{\partial \sigma_{ij}^d u_i^d}{\partial x_j^d} - \sum_{s=1}^{n_s} H_s^{0,d} \dot{\omega}_s^d, \tag{A3}$$

$$\frac{\partial\left(\rho^d Y_s^d\right)}{\partial t^d} + \frac{\partial\left(\rho^d Y_s^d u_j^d\right)}{\partial x_j^d} = \frac{\partial}{\partial x_j^d}\left(\rho^d D_s^d \frac{\partial Y_s^d}{\partial x_j^d}\right) + \dot{\omega}_s^d, \quad s = 1, 2, \ldots, n_s - 1, \tag{A4}$$

$$p^d = \rho^d R^d T^d = \rho^d \frac{R_0}{W^d} T^d, \tag{A5}$$

$$\mathcal{E}^d = \rho^d C_v^d T^d + \rho^d u_j^d u_j^d / 2, \tag{A6}$$

$$\sigma_{ij}^d = \mu^d \left(\frac{\partial u_i^d}{\partial x_j^d} + \frac{\partial u_j^d}{\partial x_i^d}\right) - \frac{2}{3} \mu^d \frac{\partial u_k^d}{\partial x_k^d} \delta_{ij}, \tag{A7}$$

$$\frac{1}{W^d} = \sum_{s=1}^{n_s} \frac{Y_s}{W_s}. \tag{A8}$$

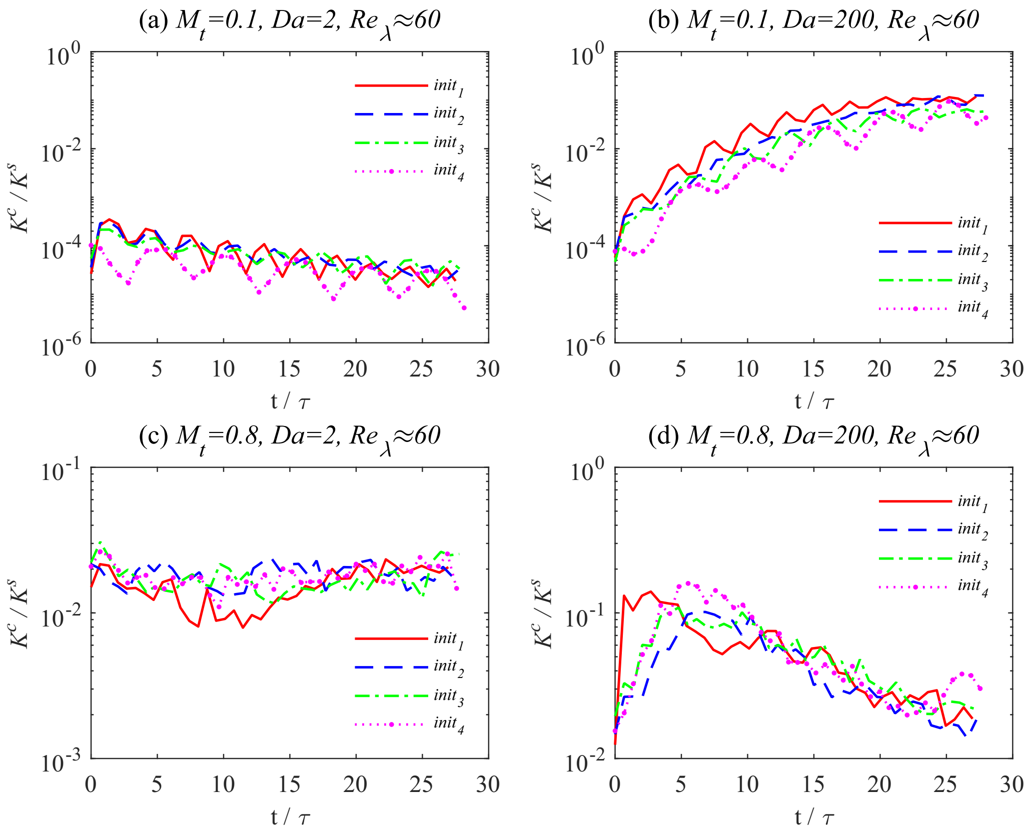

FIG. 27. Temporal variation of compressible to solenoidal kinetic energy ratio K^c/Ks at $M_t = 0.1$ and 0.8 at $\mathrm{Re}_\lambda \approx 60$ for isothermal ($\mathrm{Da} = 2$) and exothermal ($\mathrm{Da} = 200$) reactions, log-log scale. (a) $M_t = 0.1$, $\mathrm{Da} = 2$; (b) $M_t = 0.1$, $\mathrm{Da} = 200$; (c) $M_t = 0.8$, $\mathrm{Da} = 2$; (d) $M_t = 0.8$, $\mathrm{Da} = 200$.

In the equations, the variables include density ρ, velocity component u_j, time t, direction component x_j, pressure p, total energy per unit volume $\mathcal{E}$, temperature T, thermal conductivity κ, total number of species n_s, heat of reaction of sth species $-H_s^0$, reaction rate of sth species $\dot{\omega}_s$, mass fraction of sth species Y_s, mass diffusivity of sth species D_s, molecular weight of sth species W_s, total molecular weight of the mixture W, specific heat at constant pressure of the mixture C_p, specific heat at constant volume of the mixture C_v, and viscosity μ.

The dimensionless variables are introduced as follows, and the subscript "f" denotes reference variables:

$$x_j = \frac{x_j^d}{L_f}, \quad \rho = \frac{\rho^d}{\rho_f}, \quad u_i = \frac{u_i^d}{U_f}, \quad T = \frac{T^d}{T_f}, \quad p = \frac{p^d}{\rho_f U_f^2}, \quad t = \frac{t^d}{L_f/U_f}, \quad \mathcal{E} = \frac{\mathcal{E}^d}{\rho_f U_f^2}, \tag{A9}$$

$$\mu = \frac{\mu^d}{\mu_f}, \quad \kappa = \frac{\kappa^d}{\kappa_f}, \quad D_s = \frac{D_s^d}{\frac{\mu_f}{\rho_f}}, \quad R_f = \frac{R_0}{W_f}, \quad \mathrm{Sc}_s = \frac{\mu}{\rho D_s}, \tag{A10}$$

$$M = \frac{U_f}{c_f} = \frac{U_f}{\sqrt{\gamma R_f T_f}}, \quad \mathrm{Pr} = \mu_f C_{p,f}/\kappa_f, \quad \mathrm{Re} = \frac{\rho_f U_f L_f}{\mu_f}, \tag{A11}$$

$$\dot{\omega}_s = \frac{L_f \dot{\omega}_s^d}{U_f \rho_f}, \quad H_s^0 = \frac{H_s^{0,d}}{C_{p,f} T_f}, \quad W = \frac{W^d}{W_f}. \tag{A12}$$

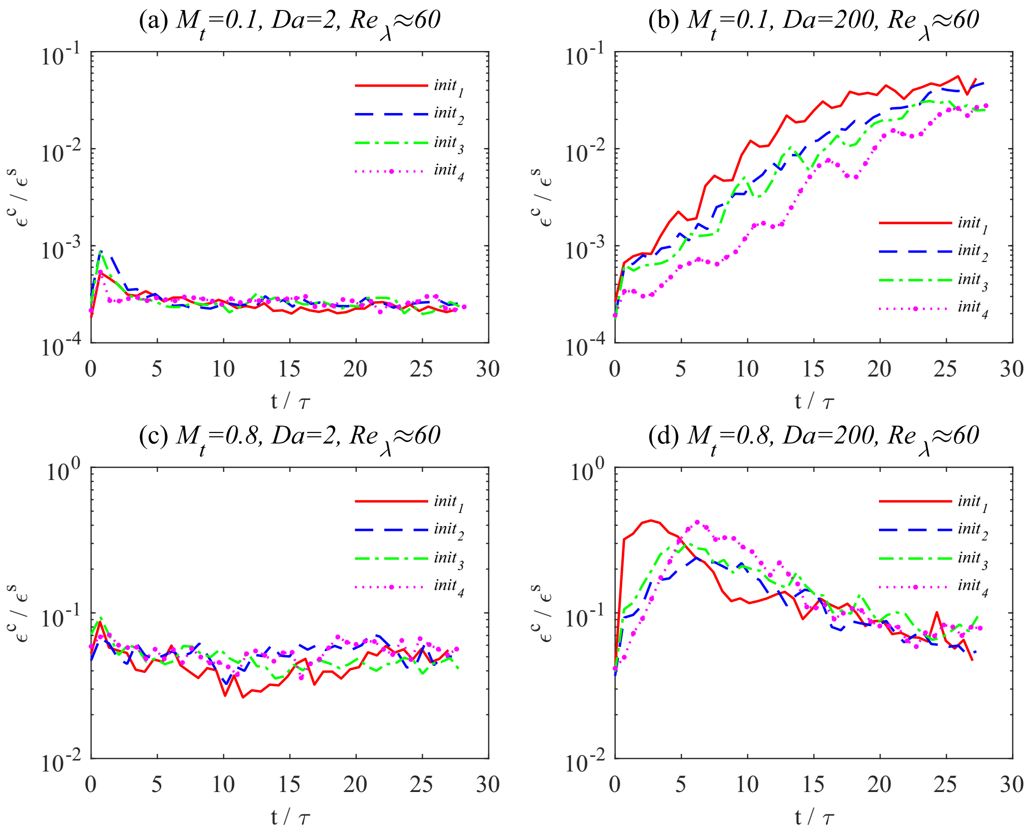

FIG. 28. Temporal variation of compressible to solenoidal dissipation rate ratio ϵ^c/ϵ^s at $M_t = 0.1$ and 0.8 at $\mathrm{Re}_\lambda \approx 60$ for isothermal (Da = 2) and exothermal (Da = 200) reactions, log-log scale. (a) $M_t = 0.1$, Da = 2; (b) $M_t = 0.1$, Da = 200; (c) $M_t = 0.8$, Da = 2; (d) $M_t = 0.8$, Da = 200.

Here R_0 denotes the universal gas constant, and R is the gas constant of the mixture. The ratio of specific heat at constant pressure to that at constant volume γ and the molecular weight of the mixture W are assumed to be unchanged during the chemical reaction process:

$$\gamma = \frac{C_{p,f}}{C_{v,f}} = \frac{C_p^d}{C_v^d}, \quad W^d = W_f. \tag{A13}$$

The Schmidt numbers for all species are assumed to be identical and can be calculated by

$$\mathrm{Sc}_s = \mathrm{Sc} = \frac{\mu_f}{\rho_f D_f}, \quad s = 1, 2, \ldots, n_s, \tag{A14}$$

where D_f is the reference mass diffusivity proportional to $T_f^{3/2}/p_f$.

Applying the current single-step irreversible reaction equation, the large-scale forcing $\mathcal{F}$, and the cooling function Λ to the N-S equations, the final dimensionless N-S equations are as follows:

$$\frac{\partial \rho}{\partial t} + \frac{\partial(\rho u_j)}{\partial x_j} = 0, \tag{A15}$$

$$\frac{\partial(\rho u_i)}{\partial t} + \frac{\partial[\rho u_i u_j + p\delta_{ij}]}{\partial x_j} = \frac{1}{\mathrm{Re}}\frac{\partial \sigma_{ij}}{\partial x_j} + \mathcal{F}_i, \quad \sigma_{ij} = \mu\left(\frac{\partial u_i}{\partial x_j} + \frac{\partial u_j}{\partial x_i}\right) - \frac{2}{3}\mu\theta\delta_{ij}, \tag{A16}$$

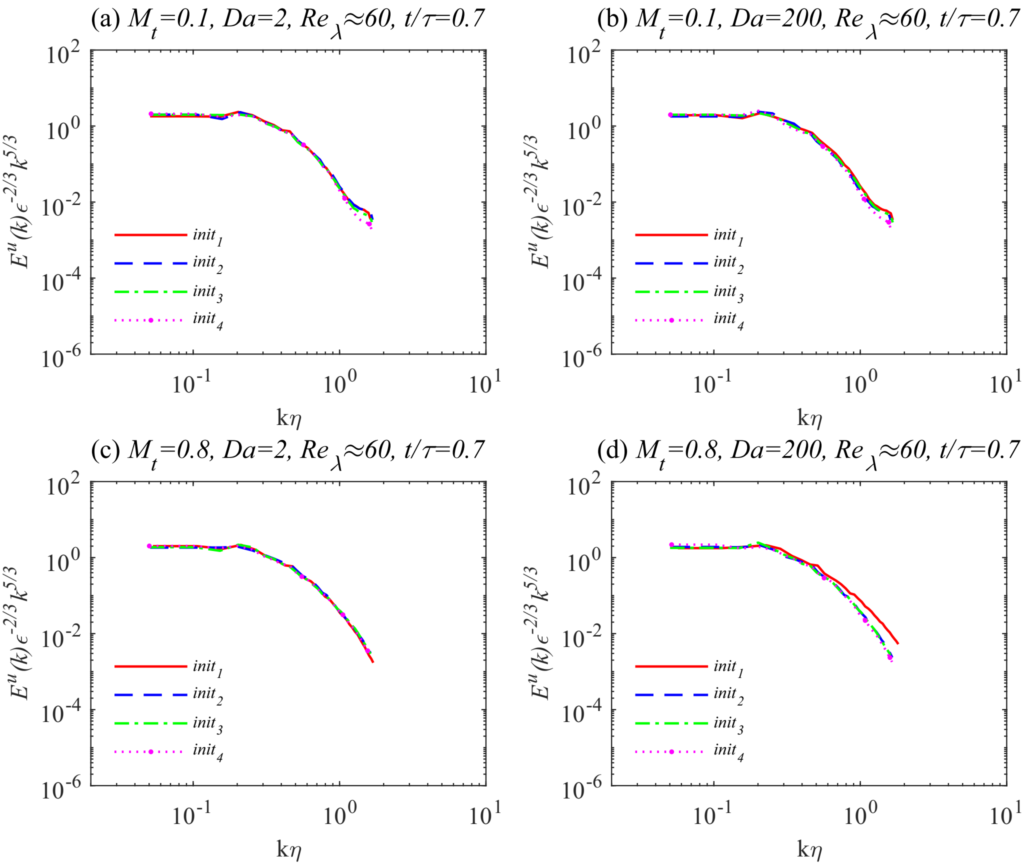

FIG. 29. Instantaneous compensated spectra of velocity $E^u(k)\epsilon^{-2/3}k^{5/3}$ at $M_t = 0.1$ and 0.8 at $\mathrm{Re}_\lambda \approx 60$ for isothermal (Da = 2) and exothermal (Da = 200) reactions at $t/\tau = 0.7$. (a) $M_t = 0.1$, Da = 2; (b) $M_t = 0.1$, Da = 200; (c) $M_t = 0.8$, Da = 2; (d) $M_t = 0.8$, Da = 200.

$$\frac{\partial \mathcal{E}}{\partial t} + \frac{\partial[(\mathcal{E}+p)u_j]}{\partial x_j} = \frac{1}{\alpha}\frac{\partial}{\partial x_j}\left(\kappa\frac{\partial T}{\partial x_j}\right) + \frac{1}{\mathrm{Re}}\frac{\partial(\sigma_{ij}u_i)}{\partial x_j} + Q - \Lambda + \mathcal{F}_j u_j, \tag{A17}$$

$$\frac{\partial(\rho Y_s)}{\partial t} + \frac{\partial(\rho Y_s u_j)}{\partial x_j} = \frac{1}{\mathrm{Re}}\frac{1}{\mathrm{Sc}}\frac{\partial}{\partial x_j}\left(\mu\frac{\partial Y_s}{\partial x_j}\right) + \dot{\omega}_s,\ s = 1, 2, \ldots, n_s - 1, \tag{A18}$$

$$p = \rho T/(\gamma M^2), \quad \mathcal{E} = \frac{p}{\gamma - 1} + \frac{1}{2}\rho(u_j u_j). \tag{A19}$$

Here the dimensionless reaction rates and heat release terms are as follows:

$$\dot{\omega}_A = -\frac{K_f \rho_f L_f}{U_f W_f^2}\rho^2 Y_A Y_B \exp\left(\frac{-Ea}{RTT_f}\right), \tag{A20}$$

$$\dot{\omega}_A = \dot{\omega}_B = -\frac{1}{2}\dot{\omega}_P, \tag{A21}$$

$$Q = \frac{-H_0/(C_{p,f}T_f)}{(\gamma - 1)M^2}\dot{\omega}_P. \tag{A22}$$

The dimensionless reaction rates and heat release terms can be rewritten as

$$\dot{\omega}_A = \dot{\omega}_B = -\frac{1}{2}\dot{\omega}_P = -\,\mathrm{Da}\,\rho^2 Y_A Y_B \exp(-\mathrm{Ze}/T), \tag{A23}$$

$$Q = \frac{\mathrm{Ce}}{(\gamma - 1)M^2}\dot{\omega}_P, \tag{A24}$$

where the Damköhler number $\mathrm{Da} = K_f \rho_f L_f/(U_f W_f^2)$, the Zeldovich number $\mathrm{Ze} = E_a/RT_f$, and the heat release parameter $\mathrm{Ce} = -H^0/C_p T_f$. K_f is the reaction rate parameter, E_a is the activation energy, and $-H^0$ is the heat of reaction.

APPENDIX B: INFLUENCE OF INITIAL DENSITY FIELDS ON FLOW STATISTICS

The influence of initial density fields on flow statistics is analyzed based on simulation data on 64^3 grid at Taylor Reynolds number $\mathrm{Re}_\lambda \approx 60$ and at turbulent Mach number $M_t = 0.1$ and 0.8 for isothermal ($\mathrm{Da} = 2$) and exothermal ($\mathrm{Da} = 200$) reactions as shown in Figs. 21–29. Four initial density fields are considered. $init_1$ initializes Y_A and Y_B homogeneously where $Y_A = Y_B = 0.5$. $init_2 \sim init_4$ use slabs for initialization, and the gray slab stands for $Y_A = 0.99$, $Y_B = 0.01$, and the white slab stands for $Y_A = 0.01$, $Y_B = 0.99$. The spatial average of Y_A and Y_B is identical, where $\langle Y_A\rangle = \langle Y_B\rangle = 0.5$ for the four initial density fields. $init_4$ is the initial density field adopted in the current paper.

The results show that the initial density field will affect the reaction rate and the product generation rate due to the time required for species mixing at the initial reaction phrase. With the increase of species slabs for initialization, the results will get close to those of idealized initialization ($init_1$). At $t/\tau > 25$, the flow statistics are slightly influenced by a different initial density field, and thus our analysis and conclusions based on flow statics at $t/\tau > 25$ have general applicability.

---

[1] P. A. Libby and F. A. Williams, *Turbulent Reacting Flows* (Springer-Verlag, Berlin, 1980).

[2] K. K. Kuo and R. Acharya, *Applications of Turbulent and Multiphase Combustion* (John Wiley & Sons, Ltd, New Jersey, 2012).

[3] P. Norbert, *Turbulent Combustion* (Cambridge University Press, Cambridge, 2000).

[4] F. A. Jaberi and C. K. Madnia, Effects of heat of reaction on homogeneous compressible turbulence, J. Sci. Comput. **13**, 201 (1998).

[5] D. Livescu, F. A. Jaberi, and C. K. Madnia, The effects of heat release on the energy exchange in reacting turbulent shear flow, J. Fluid Mech. **450**, 35 (2002).

[6] P. Paes and Y. Xuan, Numerical investigation of turbulent kinetic energy dynamics in chemically-reacting homogeneous turbulence, Flow, Turbul. Combust. **101**, 775 (2018).

[7] F. Gao and E. E. Obrien, Direct numerical simulations of reacting flows in homogeneous turbulence, AIChE J. **37**, 1459 (1991).

[8] A. D. Leonard and J. C. Hill, Mixing and chemical reaction in sheared and nonsheared homogeneous turbulence, Fluid Dyn. Res. **10**, 273 (1992).

[9] F. A. Jaberi, R. S. Miller, C. K. Madnia, and P. Givi, Non-Gaussian scalar statistics in homogeneous turbulence, J. Fluid Mech. **313**, 241 (1996).

[10] F. A. Jaberi and S. James, Effects of chemical reaction on two-dimensional turbulence, J. Sci. Comput. **14**, 31 (1999).

[11] M. P. Martin and G. V. Candler, Subgrid-scale model for the temperature fluctuations in reacting hypersonic turbulent flows, Phys. Fluids **11**, 2765 (1999).

[12] F. A. Jaberi, D. Livescu, and C. K. Madnia, Characteristics of chemically reacting compressible homogeneous turbulence, Phys. Fluids **12**, 1189 (2000).

[13] R. Knaus and C. Pantano, On the effect of heat release in turbulence spectra of non-premixed reacting shear layers, J. Fluid Mech. **626**, 67 (2009).

[14] L. Duan and M. P. Martin, Assessment of turbulence-chemistry interaction in hypersonic turbulent boundary layers, AIAA J. **49**, 172 (2011).

[15] C. Xiaoping and L. I. Xinliang, Direct numerical simulation of chemical non-equilibrium turbulent flow, Chin. Phys. Lett. **30**, 064702 (2013).

[16] A. Q. Eschenroeder, Intensification of turbulence by chemical heat release, Phys. Fluids **7**, 1735 (1964).

[17] G. Balakrishnan, S. Sarkar, and F. Williams, Direct numerical simulation of diffusion flames with large heat release in compressible homogeneous turbulence, in 31st *Joint Propulsion Conference and Exhibit*, https://arc.aiaa.org/doi/pdf/10.2514/6.1995-2375.

[18] J. C. Hill, Homogeneous turbulent mixing with chemical reaction, Annu. Rev. Fluid Mech. **8**, 135 (1976).

[19] A. D. Leonard, J. C. Hill, S. Mahalingam, and J. H. Ferziger, Analysis of homogeneous turbulent reacting flows, in *Studying Turbulence Using Numerical Simulation Databases, II*, edited by P. Moin (Center for Turbulence Research, 1988), pp. 243–255.

[20] R. Dash, Structure of the reactant and product of a turbulent second-order reaction at large wave numbers, J. Appl. Phys. **44**, 197 (1973).

[21] A. Q. Eschenroeder, Turbulence spectra in a reacting gas, AIAA J. **3**, 1839 (1965).

[22] A. Chakraborty and H. Mazumdar, On the inertial energy spectrum of turbulence in a reacting gas, Mech. Res. Commun. **14**, 317 (1987).

[23] J. Wang, Y. Shi, L. Wang, Z. Xiao, X. T. He, and S. Chen, Effect of compressibility on the small-scale structures in isotropic turbulence, J. Fluid Mech. **713**, 588 (2012).

[24] M. R. Petersen and D. Livescu, Forcing for statistically stationary compressible isotropic turbulence, Phys. Fluids **22**, 116101 (2010).

[25] D. A. Donzis and S. Jagannathan, Fluctuations of thermodynamic variables in stationary compressible turbulence, J. Fluid Mech. **733**, 221 (2013).

[26] J. R. Ristorcelli, A pseudo-sound constitutive relationship for the dilatational covariances in compressible turbulence, J. Fluid Mech. **347**, 37 (1997).

[27] S. Sarkar, G. Erlebacher, M. Y. Hussaini, and H. O. Kreiss, The analysis and modelling of dilatational terms in compressible turbulence, J. Fluid Mech. **227**, 473 (1991).

[28] J. Wang, T. Gotoh, and T. Watanabe, Spectra and statistics in compressible isotropic turbulence, Phys. Rev. Fluids **2**, 013403 (2017).

[29] J. Wang, L. Wang, Z. Xiao, Y. Shi, and S. Chen, A hybrid numerical simulation of isotropic compressible turbulence, J. Comput. Phys. **229**, 5257 (2010).

[30] S. Chen and N. Cao, Anomalous Scaling and Structure Instability in Three-Dimensional Passive Scalar Turbulence, Phys. Rev. Lett. **78**, 3459 (1997).

[31] D. A. Donzis and A. F. Maqui, Statistically steady states of forced isotropic turbulence in thermal equilibrium and non-equilibrium, J. Fluid Mech. **797**, 181.

[32] J. Wang, M. Wan, S. Chen, C. Xie, and S. Chen, Effect of shock waves on the statistics and scaling in compressible isotropic turbulence, Phys. Rev. E **97**, 043108 (2018).

[33] C.-W. Shu and S. Osher, Efficient implementation of essentially non-oscillatory shock-capturing schemes, J. Comput. Phys. **77**, 439 (1988).

[34] S. Gottlieb and C.-W. Shu, Total variation diminishing Runge-Kutta schemes, Math. Comput. **67**, 73 (1998).

[35] S. K. Lele, Compact finite difference schemes with spectral-like resolution, J. Comput. Phys. **103**, 16 (1992).

[36] D. S. Balsara and C.-W. Shu, Monotonicity preserving weighted essentially non-oscillatory schemes with increasingly high order of accuracy, J. Comput. Phys. **160**, 405 (2000).

[37] J. Wang, Y. Shi, L. Wang, Z. Xiao, X. T. He, and S. Chen, Effect of shocklets on the velocity gradients in highly compressible isotropic turbulence, Phys. Fluids **23**, 125103 (2011).

[38] J. Wang, Y. Shi, L.-P. Wang, Z. Xiao, X. T. He, and S. Chen, Scaling and Statistics in Three-Dimensional Compressible Turbulence, Phys. Rev. Lett. **108**, 214505 (2012).

[39] J. Wang, Y. Yang, Y. Shi, Z. Xiao, X. T. He, and S. Chen, Cascade of Kinetic Energy in Three-Dimensional Compressible Turbulence, Phys. Rev. Lett. **110**, 214505 (2013).

[40] J. Wang, Y. Yang, Y. Shi, Z. Xiao, X. T. He, and S. Chen, Statistics and structures of pressure and density in compressible isotropic turbulence, J. Turbul. **14**, 21 (2013).

[41] J. Wang, M. Wan, S. Chen, and S. Chen, Kinetic energy transfer in compressible isotropic turbulence, J. Fluid Mech. **841**, 581 (2018).

[42] J. Wang, M. Wan, S. Chen, C. Xie, Q. Zheng, L.-P. Wang, and S. Chen, Effect of flow topology on the kinetic energy flux in compressible isotropic turbulence, J. Fluid Mech. **883**, A11 (2020).

[43] T. Watanabe and T. Gotoh, Inertial-range intermittency and accuracy of direct numerical simulation for turbulence and passive scalar turbulence, J. Fluid Mech. **590**, 117 (2007).

[44] R. Samtaney, D. I. Pullin, and B. Kosović, Direct numerical simulation of decaying compressible turbulence and shocklet statistics, Phys. Fluids **13**, 1415 (2001).

[45] S. Jagannathan and D. A. Donzis, Reynolds and mach number scaling in solenoidally-forced compressible turbulence using high-resolution direct numerical simulations, J. Fluid Mech. **789**, 669 (2016).

[46] L. Q. Liu, J. C. Wang, Y. P. Shi, S. Y. Chen, and X. T. He, An extended hybrid numerical simulation of isotropic compressible turbulence arXiv:1711.00255.

[47] J. Wang, M. Wan, S. Chen, C. Xie, L.-P. Wang, and S. Chen, Cascades of temperature and entropy fluctuations in compressible turbulence, J. Fluid Mech. **867**, 195 (2019).

[48] G. Fauchet and J. P. Bertoglio, An analytical expression for the spectrum of compressible turbulence in the low Mach number limit, in *Advances in Turbulence VII*, edited by U. Frisch (Springer Netherlands, Dordrecht, 1998), pp. 317–320.

[49] D. Donzis, K. Sreenivasan, and P. Yeung, Some results on the Reynolds number scaling of pressure statistics in isotropic turbulence, Physica D **241**, 164 (2012), special issue on Small Scale Turbulence.

[50] J. J. Doom, Direct numerical simulation of turbulent, chemically reacting flows, Ph.D. thesis, University of Minnesota, 2009.

[51] R. Jahanbakhshi, DNS of compressible reacting turbulent shear layer, Ph.D. thesis, the State University of New York at Buffalo, 2016.